Observation and Measurement of W Boson Production and Triple Gauge Couplings at LEP II

by

Yoshiyuki Uchida

Submitted to the Department of Physics
in partial fulfillment of the requirements for the degree of

Doctor of Philosophy

at the

MASSACHUSETTS INSTITUTE OF TECHNOLOGY

Februrary 2001

© Yoshiyuki Uchida, MMI. All rights reserved.

The author hereby grants to MIT permission to reproduce and distribute publicly paper and electronic copies of this thesis document in whole or in part.

Author .....
Department of Physics
January 12, 2001

Certified by .....
Peter H. Fisher
Associate Professor
Thesis Supervisor

Accepted by .....
Thomas J. Greytak
Professor, Associate Department Head for Education

MASSACHUSETTS INSTITUTE OF TECHNOLOGY
MAR 0 4 2002
LIBRARIES
ARCHIVES

Observation and Measurement of W Boson Production and Triple Gauge Couplings at LEP II

by

Yoshiyuki Uchida

Submitted to the Department of Physics
on January 12, 2001, in partial fulfillment of the
requirements for the degree of
Doctor of Philosophy

Abstract

W-Pair and Single-W production events are observed at LEP, the Large Electron Positron collider at CERN, using the L3 detector. All decay channels are considered, and data taken in the years 1998 and 1999, with electron-positron collision centre-of-mass energies from 189 GeV to 202 GeV are analysed. The integrated luminosity of the analysed data corresponds to approximately 400pb^{-1}, and a total of approximately 5000 W-pair events and 100 single-W events are selected.

The observed cross sections of these W production processes and the differential distributions of the event shapes are then used to measure the couplings of W bosons with Z bosons and photons. Emphasis is placed on the unambiguous and efficient combination of the information from the different production and decay channels.

For the couplings in the model in which gauge invariance is realised linearly, the following results are obtained:

$$\begin{array}{lcrrll} g_1^Z & = & 0.95 & -0.03\,+0.03 & \pm 0.03 & \pm 0.03 \\ \kappa_\gamma & = & 0.91 & -0.05\,+0.05 & \pm 0.10 & \pm 0.07 \\ \lambda_\gamma & = & -0.07 & -0.03\,+0.03 & \pm 0.03 & \pm 0.03 \end{array}$$

where the errors shown are statistical, systematic and theoretical respectively.

All results show consistency with expectations from the Standard Model.

Thesis Supervisor: Peter H. Fisher
Title: Associate Professor

Contents

Introduction

With the advent of LEP II, the high energy running phase of the LEP electron positron collider at CERN, the era of heavy gauge boson pair and four fermion final state production and precision measurement was brought about. The non-commutative, or non-Abelian, structure of the Electroweak gauge group, as evidenced by the existence of couplings between gauge bosons, is one aspect of the Standard Model newly open to scrutiny at these high energies. The present thesis utilises the large amount of data that has become available since 1998, to examine gauge boson couplings at high precision using W-pair and Single-W production events at the L3 detector at LEP. Emphasis is placed on the efficient combination of these channels when extracting coupling values and a fitting method is utilised which allows the simultaneous fitting of multiple couplings while making the most of limited data and Monte Carlo statistics.

Chapter 1 — Theoretical Background

Since the era of modern physics was ushered in with the experimental discovery of β-decay at the end of the nineteenth century, many theoretical advances have contributed to form the present understanding of the structure of nature at the microscopic level. In this chapter those basic contributions which are most relevant to this thesis are outlined, followed by a discussion of the specific structure of the Weinberg-Salam Model [1,2], or the Standard Model of Electroweak Physics, centring on the gauge boson sector which is probed by the observations made here. Finally, a generalised description of massive boson interactions is given which allows the quantitative comparison of experiment to theory.

1.1 Quantum Field Theory and the Gauge Principle

Quantum field theory [3–5] was born of the need to reconcile the two new theories which had revolutionised physics at the beginning of the twentieth century, namely Special Relativity and Quantum Mechanics. It offers a framework within which to describe both the quantum mechanical nature of elementary particles in terms of probability amplitudes, and their relativistic behaviour such as creation and annihilation, which follows from the equivalence of energy and mass, a consequence of Special Relativity. Quantum field theory also contains the additional assumption that these elementary particles can be described mathematically as being fundamentally point-like, and any observed effects of finite particle size are purely due to quantum mechanical smearing. The idea of invariance, or symmetry, under Lorentz transformations, from which follow the conservation of energy and momentum and their rotational equivalents, plays a central role in the construction of this theory.

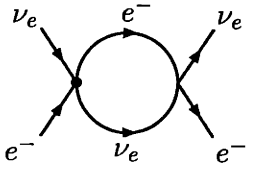

Figure 1-1: Higher order diagram for the process $\nu_e + e \to \nu_e + e$.

While at low energies (involving interactions with exchanged momenta of $\lesssim 100$ MeV), the original field theory as proposed by Fermi is able to describe experimental observations, it was clear that inconsistencies within the theory itself would necessitate its modification when applied to higher energies. One of the simplest examples of such problems is the differential cross section $d\sigma/d\Omega$ for the process $\nu_e + e \to \nu_e + e$, which has a high energy behaviour of the form

$$\frac{d\sigma}{d\Omega} = \frac{G_F^2 s}{4\pi^2} \quad \to \quad \infty \quad (s \to \infty), \tag{1.1}$$

where the dependency on the centre-of-mass energy squared s can be found from basic dimensional analysis, due to G_F having the dimension $[M]^{-2}$. For a point interaction such as this the partial wave expansion of the scattering amplitude involves only the s-wave contribution, which gives, in terms of $\mathcal{M}_0$ the s-wave matrix element,

$$\frac{d\sigma}{d\Omega} = \frac{|\mathcal{M}_0|^2}{s}. \tag{1.2}$$

Eqs. 1.1 and 1.2 clearly violate the requirement $|\mathcal{M}| \leq 1$, the conservation of probability (unitarity), above a certain high energy cutoff, which evaluates to $\sqrt{s} \approx 600$ GeV.

Additionally, each higher order calculation for the process, such as that for the diagram in Fig. 1-1, has divergences which increase in severity the higher the order, which consigns the theory to being but an effective approximation to a more fundamental theory, and only valid for low energy, low order calculations. This problem of *unrenormalisability* is unavoidable in a theory with the Fermi point interaction.

In Quantum Electrodynamics (QED), the photon acts as a mediator in the interactions of charged particles, and this provides for a renormalisable theory without the problems such as those which burden the Fermi theory. The idea that short range forces between the fermions could be mediated by massive bosons was originally suggested by Yukawa for the nuclear forces [6]. Such a particle must possess integral spin due to spin conservation at its vertex with two spin $1/2$ fermions. A construct similar to that of QED could be used for the weak interaction with a new weak boson playing the role of the mediating particle.

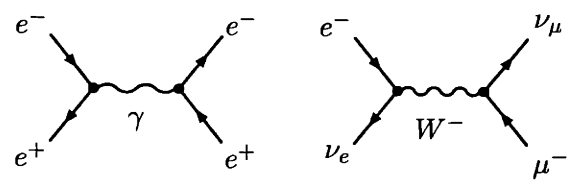

Figure 1-2: Diagrams showing the role of photons as intermediate bosons for the electromagnetic interaction, and a possible intermediate boson for the weak interaction.

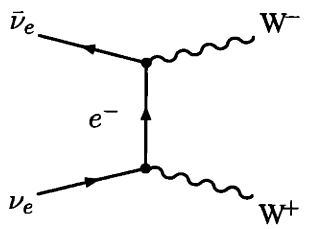

Figure 1-3: First-order Feynman diagram for a possible new process which must arise when the intermediate boson W is introduced. In pre-gauge Fermi theory, the cross section for this process diverges due to contributions from the longitudinal states of the boson.

The short range nature of the weak interaction would require that such an intermediate weak boson has a large mass, and indeed with this modification the total cross section for $\nu_e + e \rightarrow \nu_e + e$ approaches a finite constant value $G_F^2 M_W^2/\pi$ as $s \rightarrow \infty$. Nevertheless, the s-wave amplitude is now

$$\mathcal{M}_0 = \frac{G_F M_W^2}{\sqrt{2}\pi} \log\left(1 + \frac{s^2}{M_W^2}\right),$$

which fails the unitarity requirement, albeit at extremely high energies ($\sqrt{s} \gtrsim 10^{12}$ GeV if one takes $M_W \approx 80$ GeV).

The situation is still worse, for if one calculates the amplitudes for diagrams with internal loops involving an intermediate weak boson with momentum q, the propagator term $(-g_{\mu\nu} + q_\mu q_\nu / M_W^2)/(q^2 - M_W^2)$ tends to a constant as $q^2 \rightarrow \infty$, causing divergences again when integration over loops is performed. In addition, a massive vector boson would have longitudinal polarisation states in addition to the transverse states found in a massless boson, and the cross section for the process (Fig. 1-3)

$$\nu_e + \bar{\nu}_e \quad \rightarrow \quad W^+ + W^-$$

with W^+ and W^- representing the positively charged weak vector boson and its antiparticle respectively, would have a finite contribution from the transverse final states, but longitudinal $W^\pm$ production would have a divergent cross section $\sigma \propto k^2$, where k is the W momentum. This can

be seen from the longitudinal polarisation vector $\epsilon_{\rm L}$, which in a rest frame with the z-axis in the W direction such that the momentum $k^\mu = (k^0, 0, 0, k)$, can be written

$$\epsilon_{\rm L} = \left(|\boldsymbol{k}|/M_{\rm W}, 0, 0, k^0/M_{\rm W}\right) = k^\mu/M_{\rm W} + \mathcal{O}(M_{\rm W}/k^0). \tag{1.3}$$

The transverse polarisation vectors are independent of the boson momentum. From these arguments, it can be seen that an additional massive gauge boson to mediate the weak interaction possesses promising properties, but in this simple form it still is not free of problems which preclude it from being part of a satisfactory description of the weak interaction.

The principle of Gauge Invariance was introduced to rectify the situation, and takes the concept of invoking symmetry principles to guide the construction of theories one step further, by introducing another class of symmetry, that of symmetry under local gauge, or phase, transformations [7].

In general, the principle of gauge invariance for a field theory describing the dynamics of a field $\varphi(x)$ involves selecting a gauge group G and imposing the requirement that the theory is unchanged under the transformation

$$\varphi(x) \rightarrow \varphi'(x) \quad = \quad e^{-i\boldsymbol{L}\cdot\boldsymbol{\theta}(x)}\varphi(x), \tag{1.4}$$

where $\boldsymbol{L} = (L_1, \ldots, L_{N_G})$, where L_j is a set of square matrices representing the group G, and $\boldsymbol{\theta}(x) = (\theta_1(x), \ldots, \theta_{N_G}(x))$, where $\theta_j(x)$ are arbitrary functions. QED was the first example of a working gauge theory, with the behaviour of the photon field under gauge transformations emerging when invariance under Eq. 1.4 is imposed with U(1) as the choice of gauge group G. The covariant derivative (Eq. 1.5), which gives the changes in the field in both internal gauge space and external space-time, is introduced to render invariant the terms in the Lagrangian containing derivatives of $\varphi(x)$, and $A_\mu(x)$ is interpreted as the photon field, resulting in the photon interaction described in the first term of Eq. 1.6.

$$D_\mu^{(j)} \equiv \partial_\mu + i\,e\,q_j A_\mu, \tag{1.5}$$

$$\mathcal{L}_\gamma = \bar{\varphi}\left(i\gamma^\mu D_\mu^{(j)} - m_j\right)\varphi - \tfrac{1}{4}F_{\mu\nu}(x)F^{\mu\nu}(x). \tag{1.6}$$

The kinetic term for the photon is written using the field strength tensor $F_{\mu\nu} = \partial_\mu A - \partial_\nu A$ which guarantees gauge invariance for this term.

In the case where G is a more general group, by introducing the covariant derivative in analogy with QED,

$$D_\mu = \partial_\mu + i\,g\boldsymbol{L}\cdot\boldsymbol{W}_\mu, \tag{1.7}$$

with the new gauge boson field $\boldsymbol{W}_\mu$ transforming as

$$W_\mu^j(x) \rightarrow W'^j_\mu \equiv W_\mu^j(x) + \frac{1}{g}\partial_\mu\theta_j(x) + c_{jkl}\theta_k(x)W_\mu^l(x), \tag{1.8}$$

where c_{jkl} are the structure constants of G, and including the kinetic energy terms of the new gauge boson field

$$\mathcal{L}_{\boldsymbol{W}}^{\rm kin} = -G_{\mu\nu}^j G^{j,\mu\nu}, \tag{1.9}$$

where

$$G_{\mu\nu}^j = \partial_\mu W_\nu^i - \partial_\nu W_\mu^j + g\,c_{jkl}W_\mu^k W_\nu^l, \tag{1.10}$$

the Lagrangian remains gauge invariant, and provides a consistent theory, with specific forms for the interactions among the fermions and the new gauge bosons. Crucially, the expressions for the term in the Lagrangian for the new gauge bosons show that if the group initially chosen to express the gauge transformation is non-Abelian, ie, non-commutative, the c_{jkl} term in Eq. 1.10 indicates the existence of self-couplings between the new gauge fields $\boldsymbol{W}_\mu$.

The gauge principle allows the construction of a Lagrangian which incorporates gauge bosons which mediate interactions between matter particles, whose structure is guided by the choice of group which describes the nature of the gauge symmetry of the theory. The choice of group is not constrained by the theory, and by comparison with experiment, one can rule out or favour certain choices. In its original formulation, the gauge principle does not allow for massive gauge bosons, and combined with the fact that the mass terms for the fermions in the theory do not necessarily satisfy gauge invariance, in this form it cannot satisfactorily be applied as a valid description of nature.

The concepts of Spontaneous Symmetry Breaking [8,9] and the Higgs Mechanism [10–12] allow the introduction of mass terms to the Lagrangian while maintaining gauge invariance. This procedure also produces terms describing additional scalar particles, the Higgs bosons, currently the subject of intense experimental effort and for which candidate events have been observed recently at L3 [13]. The specific expressions within the SM for these additional terms which complete the description of the gauge bosons are discussed in the following chapter.

1.2 The Standard Model of Electroweak Interactions

The principle of gauge invariance can be applied to quantum field theory to construct consistent quantum models with interacting particles. The properties of the models are given by the choice of gauge group G, with the number of generators possessed by this group defining the number of gauge fields, and the matter fields, whose representations determine how they transform under G. Interactions with scalar fields in a Lagrangian which introduces spontaneous symmetry breaking allow some of the vector bosons to acquire mass.

The Standard Model is one particular example of such a theory, with the best known choice of input parameters. The present analysis acts to test directly the validity of the assumption of gauge invariance and the choice of input parameters which determine the structure of the model, which will be summarised in this chapter.

Structure

The gauge group of the Standard Model of Electroweak Interactions (SM) is $\mathrm{SU}(2)\times\mathrm{U}(1)$, which has four generators. Historically, the suitability of the $\mathrm{SU}(2)\times\mathrm{U}(1)$ group to describe the electromagnetic and weak interactions was noticed in the early 1960's [14,15], and it was not until later in the decade [1,2] that it was shown that massive gauge fields could be incorporated into the theory using the Higgs mechanism. The four vector bosons resulting from this choice of gauge group ultimately should be identified with the single massless intermediate boson of QED and three massive weak interaction bosons. Of the many possibilities for the structure of the scalar fields, the simplest consists of a weak isodoublet

$$\phi = \begin{pmatrix} \phi^+ \\ \phi^0 \end{pmatrix} \tag{1.11}$$

of charged and neutral complex scalar fields, with the scalar potential

$$V(\phi^\dagger\phi) = \mu^2\phi^\dagger\phi + \lambda(\phi^\dagger\phi)^2.$$

For $\mu^2 < 0$ and $\lambda > 0$, the vacuum state of the system can occur at any of a continuous range of points ϕ which satisfy $|\phi|^2 = -\mu^2/2\lambda$, where the potential is at its minimum. This choice for the Higgs sector parameters corresponds to what is known as the Minimal SM. While the Lagrangian remains gauge invariant, the symmetry does not manifest itself at each of the possible vacuum points, implying that spontaneous symmetry breaking takes place. The vacuum state of the system can be

chosen to be at

$$\phi_0 = \begin{pmatrix} 0 \\ v/\sqrt{2} \end{pmatrix},$$

where $v = \sqrt{-\mu^2/\lambda}$.

The vector bosons $\boldsymbol{W}$ and B_μ interact with the scalars through the following terms in the Lagrangian:

$$\mathcal{L}_{V\phi} = (D_\mu\phi)(D^\mu\phi^\dagger) = \left\{(\partial_\mu + i\frac{g}{2}\boldsymbol{W}_\mu\cdot\boldsymbol{\tau} + i\frac{g'}{2}IB_\mu)\phi\right\} \times \left\{\ldots\right\}^\dagger \tag{1.12}$$

The four 2×2 matrices $\boldsymbol{\tau}$ and I represent the generators of SU(2) and U(1), and are the three Pauli matrices and the unit matrix respectively. The gauge fields can be redefined as

$$A_\mu = \cos\theta_w B_\mu + \sin\theta_w W^3_\mu, \quad Z_\mu = \sin\theta_w B_\mu - \cos\theta_w W^3_\mu, \tag{1.13}$$

where θ_w is the weak mixing angle, then if $\tan\theta_w = g'/g$, it can be seen that A_μ couples to the scalar field through the generator $(I+\tau_3)/2$ of the group $\mathrm{SU(2)}\times\mathrm{U(1)}$ which leaves the vacuum invariant, thereby allowing A_μ to remain massless after spontaneous symmetry breaking. For this to be identified with the photon, the coupling between ϕ^+ and A_μ, $g\sin\theta_w$, should be equated with e, the unit electric charge. Z_μ is to be identified as a neutral gauge boson, which had not been observed at the time the SM was proposed.

Similarly, $\mathrm{W}^\pm_\mu$, defined as $(W^1_\mu \mp iW^2_\mu)/\sqrt{2}$, correspond to fields with charge ± 1, and the masses of these fields and Z_μ can be evaluated directly by substitution into Eq. 1.12, which gives $M_\mathrm{W} = gv/2$, and $M_\mathrm{Z} = gv/2\cos\theta_w$. Of the four degrees of freedom available in ϕ (Eq. 1.11), three are thus absorbed as the longitudinally polarised components of the three newly massive gauge fields. The fourth remains as the real scalar Higgs field H, with mass $M_H = \sqrt{-2\mu^2}$, a free parameter.

Matter Fields

The fact that the gauge group $\mathrm{SU(2)}\times\mathrm{U(1)}$ of the SM is non-Abelian implies the existence of self-interactions of the gauge bosons. These are described by Eqs. 1.6, 1.9 and 1.8, with the substitutions of Eq. 1.13, and are examined in detail in Section 1.3. The rich phenomenology of matter fields are described in the SM in terms of the representations of the fields and coupling constants and masses. In this section, the most pertinent aspects which in relation to the gauge interactions of these fields is briefly characterised.

The $\mathrm{U(1)_{em}}$ structure of QED requires that all particles possess a charge quantum number q which determines the dependence of the fields on gauge transformations, and ultimately, their couplings with the gauge fields. Similarly, the $\mathrm{SU(2)}\times\mathrm{U(1)}$ structure of the SM electroweak sector gives rise to three charge-like quantum numbers, which are found by experiment, and which can be used to help classify the particles according their properties. The quantum number corresponding to the U(1) interaction is referred to as the weak hypercharge Y, while the charge for the SU(2) interaction is the weak isospin, being characterised by two numbers (I_W, I_{3W}) in analogy with the quantum numbers for traditional SU(2) spin in space-time.

In terms of weak isospin, the matter fields are taken to be comprised of left-handed doublets and right-handed singlets,

$$\ell_\mathrm{L} \equiv \begin{pmatrix} \nu_e \\ e \end{pmatrix}_\mathrm{L}, \; e_\mathrm{R} \qquad q_\mathrm{L} \equiv \begin{pmatrix} u \\ d \end{pmatrix}_\mathrm{L}, \; u_\mathrm{R}, \; d_\mathrm{R}$$

where only the first generation leptons and quarks are shown. The doublets possess weak isospin $(1/2, \pm 1/2)$, and the singlets $(0, 0)$. This choice of representation, where the neutrino only exists in

left-handed form, implies the masslessness of neutrinos, which is disputed by recent experimental results [16], but physics at LEP is insensitive to the existence of small neutrino masses.

The gauge bosons and the leptons interact according to the Lagrangian density

$$\mathcal{L} = \bar{\ell}_{\rm L} i\gamma^\mu(\partial_\mu - i\,g'B_\mu/2 + i\,g\boldsymbol{\tau}\cdot\boldsymbol{W}_\mu/2)\ell_{\rm L} + \bar{e}_{\rm R} i\,\gamma^\mu(\partial_\mu - i\,g''B_\mu)e_{\rm R}. \tag{1.14}$$

where the identification $g'' = g'$ can be made to give the same electromagnetic coupling to the right-handed electron as the left-handed electron. The definition (Eq. 1.13) of the mixing of the neutral bosons gives the relation $q = Y + I_{3W}$ between the underlying $\mathrm{SU(2)\times U(1)}$ quantum numbers and the electromagnetic charge q. Similar relations can be given for the quark interactions with the gauge bosons. The weak hypercharge assignments are then $Y(\ell_{\rm L}) = -1/2, Y(e_{\rm R}) = -1, Y(q_{\rm L}) = 1/3, Y(u_{\rm R}) = 4/3, Y(d_{\rm R}) = -2/3$.

The electron mass term $m_e(\bar{e}_L e_R + \bar{e}_R e_L)$, would not be gauge invariant by itself since e_L and e_R transform differently*. Instead the lepton-scalar interaction term

$$\mathcal{L}_{\ell\phi} = -G_e[(\bar{\ell}_L \phi e_R + \bar{e}_R \phi^\dagger \ell_L)]$$

produces the term $-(G_e v/\sqrt{2})(\bar{e}_L e_R + \bar{e}_R e_L)$ at the spontaneous symmetry breaking non-zero vacuum value v for ϕ, giving the electron a finite mass while maintaining gauge invariance. This mass includes a free parameter G_e, thus is not predicted in the SM, nevertheless it can be seen from this expression that the Higgs-fermion couplings are proportional to the fermion masses.

By comparing this theory to the Fermi theory in the extreme low energy limit, the new parameters can be written in terms of those of the old theory. For example, by comparing the coupling between $\ell_{\rm L}$ and W_μ with the Fermi coupling between charged leptons and neutrinos, an expression for g can be found:

$$\frac{g^2}{8M_{\rm W}^2} = \frac{G_{\rm F}}{\sqrt{2}} \tag{1.15}$$

The muon lifetime, which is extremely well measured, allows $G_{\rm F}$ to be evaluated as $1.16639(1) \times 10^{-5}$ GeV [17]. The vacuum v for the scalar field is then $v^2 = 1/\sqrt{2}G_{\rm F} = 246.2186$ GeV. The mass of the Z boson is predicted by the SM to be $M_{\rm Z} \simeq 74/\sin 2\theta_w$ GeV.

A similar expression to Eq. 1.12 can be written for the quark-gauge boson interaction using the appropriate coefficients to represent the transformation properties of the fields.

The relations discussed above are derived from tree level calculations, and for comparison with experiment, the appropriate higher-order corrections must be included [18].

1.3 Triple Gauge Boson Couplings

The Standard Model predicts the existence of heavy bosons Z and W of mass $\lesssim 100$ GeV, a property of the theory which was shown to be correct in spectacular fashion at the CERN $p\bar{p}$ collider in the early 1980's [19,20]. Once these particles were discovered, the experimental effort moved to the measurement of the properties of these particles such as their mass, width, cross sections and decay branching ratios. The experiments at LEP and the Tevatron have devoted many years to their study. In addition to the existence of these particles, the SM also predicts that they couple directly with each other, in the form of triple- and quadruple- gauge boson couplings. The form of this coupling is tightly constrained within the model due to the structure of the $\mathrm{SU(2)\times U(1)}$ symmetry group, as outlined in the previous sections. From an experimental perspective, it is important that the nature of the couplings is investigated and compared to the predictions of the SM. The framework

*The left and right handed fields transform as $\ell_{\rm L} \to e^{-i\boldsymbol{\tau}\cdot\boldsymbol{\theta}(x)/2}\ell_{\rm L}$, $e_{\rm R} \to e^{i\theta(x)}e_{\rm R}$ due to gauge invariance.

for conducting this comparison and the notation in general use are introduced in this section. First the most general parametrisation possible for couplings between bosons is given, not subject to the restrictions placed by the SM. Comparison of this form with that calculated within the SM allows one to describe the SM couplings using the parameters of the general case, and provides a basis for measuring the actual couplings which exist in observed reality in terms of their deviation from the SM predictions. Finally, some arguments for reducing the number of free parameters are described, which allow the investigation of the nature of these deviations under various theoretical assumptions.

The most general Lagrangian [21,22] containing terms up to dimension six, which describe interactions between three gauge bosons assuming only Lorentz invariance, can be written

$$\begin{aligned}\mathcal{L}_{WWV} = \; & g_{WWV}\Big[i\,\boldsymbol{g_1^V}\left(W^\dagger_{\mu\nu}W^\mu V^\nu - W^\dagger_\mu V_\nu W^{\mu\nu}\right) + i\,\boldsymbol{\kappa_V} W^\dagger_\mu W_\nu V^{\mu\nu} \\ & + \frac{i\,\boldsymbol{\lambda_V}}{M_{\mathrm{W}}^2} W^\dagger_{\lambda\mu} W^\mu{}_\nu V^{\nu\lambda} \\ & - \boldsymbol{g_4^V} W^\dagger_\mu W_\nu\left(\partial^\mu V^\nu + \partial^\nu V^\mu\right) \\ & + \boldsymbol{g_5^V}\,\epsilon^{\mu\nu\rho\sigma}\left(W^\dagger_\mu \overleftrightarrow{\partial_\rho} W_\nu\right) V_\sigma + i\,\tilde{\boldsymbol{\kappa}}_{\boldsymbol{V}} W^\dagger_\mu W_\nu \tilde{V}^{\mu\nu} \\ & + \frac{i\,\tilde{\boldsymbol{\lambda}}_{\boldsymbol{V}}}{M_{\mathrm{W}}^2} W^\dagger_{\lambda\mu} W^\mu{}_\nu \tilde{V}^{\nu\lambda}\Big].\end{aligned} \tag{1.16}$$

The standard notation of [21] is followed here, with V standing for either γ or Z. The values for $g_{WW\gamma}$ and g_{WWZ} are defined as being e and $e\cot\theta_W$ respectively, where θ_W is the weak mixing angle. Seven couplings for each neutral boson

$$g_1^V,\ \kappa_V,\ \lambda_V,\ g_4^V,\ g_5^V,\ \tilde{\kappa}_V,\ \tilde{\lambda}_V \tag{1.17}$$

accommodate all possibilities of WWV interactions, up to terms proportional to M_e/M_{Z} for the WWZ couplings. From 'naive dimensional analysis' [23] , the deviation of couplings from SM predictions is expected to be of $\mathcal{O}((M_{\mathrm{W}}/\Lambda_{\mathrm{NP}})^{d-4})$ where d is the dimension of the operator to which the coupling belongs, and Λ_{NP} is the energy scale of new physics. Therefore any anomalous effects are most likely to occur first in the terms in the above Lagrangian. This argument is valid for $\Lambda_{\mathrm{NP}} \gg M_{\mathrm{W}}$. All higher order operators can be constructed by replacing V^μ by $(\partial^2)^n V^\mu (n = 1, 2, \ldots)$. For comparison, the SM Lagrangian for the gauge bosons is

$$\begin{aligned}\mathcal{L}_{\mathrm{SM}} = \; & g_{WW\gamma}\Big[i\,\boldsymbol{g_1^\gamma}\left(W^\dagger_{\mu\nu}W^\mu\gamma^\nu - W^\dagger_\mu\gamma_\nu W^{\mu\nu}\right) + i\,\boldsymbol{\kappa_\gamma} W^\dagger_\mu W_\nu \gamma^{\mu\nu}\Big] \\ & + g_{WWZ}\Big[i\,\boldsymbol{g_1^Z}\left(W^\dagger_{\mu\nu}W^\mu Z^\nu - W^\dagger_\mu Z_\nu W^{\mu\nu}\right) + i\,\boldsymbol{\kappa_Z} W^\dagger_\mu W_\nu Z^{\mu\nu}\Big],\end{aligned}$$

where the symbols for the couplings have been retained for clarity, but in the SM g_1^γ, κ_γ, g_1^Z, κ_Z all equal unity. The other couplings in Eq. 1.16 vanish in the SM, and for ease of comparison, the quantities $\Delta g_1^\gamma \equiv g_1^\gamma - 1$, $\Delta\kappa_\gamma \equiv \kappa_\gamma - 1$, etc., are commonly used when discussing deviations of couplings from their SM values.

The couplings in Eq. 1.17 and the operators related to them have the following static characteristics:

$$\begin{aligned}
\text{W}^+ \text{ boson charge } Q_{\text{W}+} &= e\,g_1^\gamma \\
\text{magnetic dipole moment } \mu_{\text{W}+} &= e\,(g_1^\gamma + \kappa_\gamma + \lambda_\gamma)/2M_{\text{W}} \\
\text{electric quadrupole moment } q_{\text{W}+} &= e\,(\lambda_\gamma - \kappa_\gamma)/M_{\text{W}}^2 \\
\text{electric dipole moment } d_{\text{W}+} &= e\,(\tilde{\kappa}_\gamma + \tilde{\lambda}_\gamma)/2M_{\text{W}} \\
\text{magnetic quadrupole moment } \tilde{Q}_{\text{W}+} &= e\,(\tilde{\lambda}_\gamma - \tilde{\kappa}_\gamma)/M_{\text{W}}^2
\end{aligned}$$

$$\begin{aligned}
\text{C, P conserving couplings:} &\quad g_1^\gamma,\ \kappa_\gamma,\ \lambda_\gamma,\ g_1^{\text{Z}},\ \kappa_{\text{Z}},\ \lambda_{\text{Z}}, \\
\text{C, P violating, CP conserving couplings:} &\quad g_5^\gamma,\ g_5^{\text{Z}} \\
\text{C, P, CP violating couplings:} &\quad g_4^\gamma,\ \tilde{\kappa}_\gamma,\ \tilde{\lambda}_\gamma,\ g_4^{\text{Z}},\ \tilde{\kappa}_{\text{Z}},\ \tilde{\lambda}_{\text{Z}}
\end{aligned}$$

For on-shell photons, the known electric charge of the W fixes g_1^γ to unity, and electromagnetic gauge invariance fixes g_5^γ to 0. Constraints on coupling values from atomic measurements have been obtained [24] using the above relations for the electromagnetic properties of the W boson.

In studies prior to LEP II running, the final LEP II accuracy for direct TGC measurements was determined not to be better than $\mathcal{O}(10^{-2})$ [25,26]. The discussion in this section regarding expected SM values for the couplings are based on tree-level calculations; this is justified from studies of SM loop order corrections which show that these are of $\mathcal{O}(10^{-3})$ [27]. Other naming schemes which have been proposed and used extensively to describe gauge boson couplings are summarised in Appendix A. The LEP II TGC group produced a report with a detailed review of the properties of these couplings [25].

As has been shown in the preceding sections, the precise values of the couplings of gauge bosons with each other are predicted by the SM, and any deviations from these values would indicate that inconsistencies exist which originate at the level of Eq. 1.12, which is a direct consequence of the gauge structure of the model. The renormalisability of the theory depends crucially on the gauge invariant nature of the Lagrangian [28], hence even small deviations indicate that new mechanisms must come into play at a certain cutoff energy to allow the theory to be applicable at such high energies and beyond.

The full set of couplings is too large for useful constraints to be found simultaneously with the data available at LEP II [29–31]; therefore it is useful to constrain the number of couplings to be fitted by making use of reasonable restricting arguments on the effects of possible new physics. This can be achieved by assuming that gauge invariance holds for the whole Lagrangian, including terms which are due to new physics. Although this in itself does not provide any constraints since it is possible to make any of the non-SM coupling terms in Eq. 1.16 gauge invariant if appropriate higher order new physics terms are added, the additional requirement that only four and six dimensional operators come into play at these energies reduces the number of couplings which need to be considered. This last condition corresponds to the new physics scale being at 1 TeV or more.

When $\text{SU}(2)\times\text{U}(1)$ gauge symmetry is assumed for new physics in this way, two possibilities emerge, depending on whether a light Higgs ($M_{\text{H}} \lesssim 400$ GeV) exists.

If such a Higgs exists, any new physics which occurs at energies of above 1 TeV induces interaction terms between the Higgs and gauge boson fields in the effective Lagrangian at the electroweak scale, which can be evaluated using the vacuum expectation value for the Higgs field, in what is called the *linear* realisation of the Nambu-Goldstone bosons. A general form of the Lagrangian is assumed at a high energy scale Λ, which obeys $\text{SU}(2)\times\text{U}(1)$ gauge invariance, and the effective Lagrangian at the electroweak scale is obtained by integrating out the new heavy degrees of freedom.

Any new terms which would have produced sizable effects at propagator level [32] would have in turn produced measurable deviations in low-energy experiments and at LEP I, and can be removed from consideration. Three operators remain in the effective Lagrangian [33], with the $SU(2) \times U(1)$ covariant derivative D_μ defined as in Eq. 1.12:

$$\mathcal{O}_{WWW} = -i\,3\,g^3 W^+_{\mu\nu} W^{-\nu\rho} W^{3\,\mu}_{\rho}/2, \quad \mathcal{O}_B = i\,g(D_\mu\phi)^\dagger B^{\mu\nu}(D_\nu\phi)/2, \qquad (1.18)$$
$$\mathcal{O}_W = i\,g'(D_\mu\phi)^\dagger \boldsymbol{\tau}\cdot \boldsymbol{W}^{\mu\nu}(D_\nu\phi)/2.$$

When the Higgs vacuum expectation value is inserted, and the resulting Lagrangian compared to Eq. 1.16, the set of couplings $\{\Delta g_1^Z,\ \Delta\kappa_\gamma,\ \lambda_\gamma\}$ remains non-zero, with the relations

$$\Delta\kappa_\gamma = (\cos^2\theta_W/\sin^2\theta_W)(\Delta g_1^Z - \Delta\kappa_Z) \qquad (1.19)$$
$$\lambda_\gamma = \lambda_Z \qquad (1.20)$$

holding due to the assumption that Λ is very high and only dimension six terms need be considered in the effective Lagrangian. It should be noted that under these assumptions, the scale of new physics can be arbitrarily high, since the inclusion of a Higgs scalar field renders the theory renormalisable without the inclusion of new physics dynamics.

If the Higgs is very heavy or does not exist as a scalar resonance, a *non-linear* realisation of the Goldstone bosons is more appropriate [34], where only the degrees of freedom of the Higgs field which contribute to the longitudinal gauge bosons are evident at the electroweak scale. Some new physics must appear below roughly 3 TeV, otherwise unitarity is violated at this energy. In this scenario, the operators corresponding to the λ_V couplings are suppressed and the set of couplings $\{\Delta g_1^Z,\ \Delta\kappa_\gamma,\ \Delta\kappa_Z,\ g_5^Z\}$ are found to be the most likely to show the effects of new physics.

The above arguments notwithstanding, it is important also to retain a more open minded approach and fit combinations of the couplings without any additional constraints. In Chapter 5 the results of such fits are presented alongside the more traditional constrained fits.

There are many arguments regarding the indirect constraints that can be put on anomalous gauge boson couplings, which are discussed in the references cited in this section [35]. General phenomenological constraints are smaller than $\mathcal{O}(0.1)$ if the effect of individual couplings are evaluated one at a time, but in the more general case where more than one coupling deviates from the SM, the possibility of unknown cancellations weakens the limits to $\mathcal{O}(1)$ [30], and only through direct measurement can this uncertainty be resolved.

Chapter 2 — The L3 Experiment at LEP

The present analysis is conducted at the L3 detector at LEP, the Large Electron Positron collider at CERN in Geneva, Switzerland. In this chapter the collider and the experimental setup, and the use of the signals from the various L3 subdetectors in identifying and measuring jets and particles are briefly described. Extensive descriptions of the detector can be found elsewhere [36].

2.1 LEP

The Large Electron Positron Collider (LEP) was commissioned in 1989 to generate electron-positron collisions at high energies (Fig. 2-1). It is the largest particle accelerator in the world at approximately 27km in circumference. Electrons and positrons are the lightest charged particles, which implies that the amount of synchrotron radiation, the electromagnetic radiation given off by charged particles under acceleration, becomes a dominant design consideration at high energies.

The power lost due to synchrotron radiation has the dependency $P_{\text{sync}} \propto E_{\text{beam}}^4 \cdot R^{-1}$, on the beam energy and radius*, hence the large size of LEP, and the need to use increasingly large numbers of sophisticated accelerating RF cavities in order to reach higher energies. The previous generation accelerators, PS and SPS are used to accelerate the particles to 22 GeV prior to injection into LEP. As opposed to hadron colliders which are well suited to the initial discovery of new particle production, the well defined initial and final states and centre-of-mass energies of electron-positron colliders provide an environment which meets the requirements for precision studies of these particles, and for searches for particles which are expected to appear in events with relatively more subtle signatures.

Parameter	LEP I Average
M_Z (GeV)	91.1871±0.0021
Γ_Z (GeV)	2.4944±0.0024
σ_{hadr} (nb)	41.544±0.037
$\Gamma_{\text{hadr}}/\Gamma_{\ell\ell}$	20.768±0.024
$A_{\text{FB}}^{0,\ell}$	0.01701±0.00095
N_ν	2.994±0.012

Table 2.1: Some electroweak results from LEP I [37], averaged among the four LEP experiments.

$E_{\text{c.m.}}$ (GeV)	Years	Int. Lumi. (pb^{-1})
130	'95 / '97	6.1
136		5.9
161	'96	10.9
172		10.3
183	'97	55.5
189	**'98**	**176.8**
192		**29.7**
196		**83.7**
200	**'99**	**82.8**
202		**37.0**
204		0.037

Table 2.2: Centre-of-mass energies and integrated luminosities collected by L3 between 1995 and 1999. Over this period, the number of superconducting accelerating cavities in LEP has doubled. The data used for this analysis are shown in boldface.

LEP I ran at around the Z mass for six years, with a total of 3.7 million Z decay events being observed by L3. The central physics results are summarised in Table 2.1. Since the latter half of 1995, LEP moved into its second phase of running, LEP II [39], with the installation of new superconducting accelerating cavities allowing the collision energy to be raised first to 130 GeV, and then above the W-pair production threshold of 161 GeV in 1996, and steadily up to 204 GeV in 1999. The luminosities collected, a proportionality factor corresponding to the number of events expected for each unit reaction cross section, increased from roughly 10 pb^{-1} to over 200 pb^{-1} in 1999. The integrated luminosities collected at LEP II are summarised in Table 2.1. The data used here were collected by the L3 detector in 1998 and 1999, and correspond to centre-of-mass energies from 189 GeV to 204 GeV. More details will be presented in the analysis chapters.

2.2 The L3 Detector

L3 is one of four experiments situated at equidistant locations along the LEP ring which observe the particles produced in collisions between the two beams, whose orbits are guided into each other's paths at these four points (Fig. 2.2). In this section the detector will be described in terms of the qualities of the different types of information that its various components provide and how they allow the determination of the nature of the collisions occurring at the centre of the detector.

*For electrons the energy loss per turn can be written $8.85 \times 10^{-5} E^4/R$ MeV, with E in GeV and R in km [38], corresponding to 1700 MeVper turn at beam energies of 100 GeV.

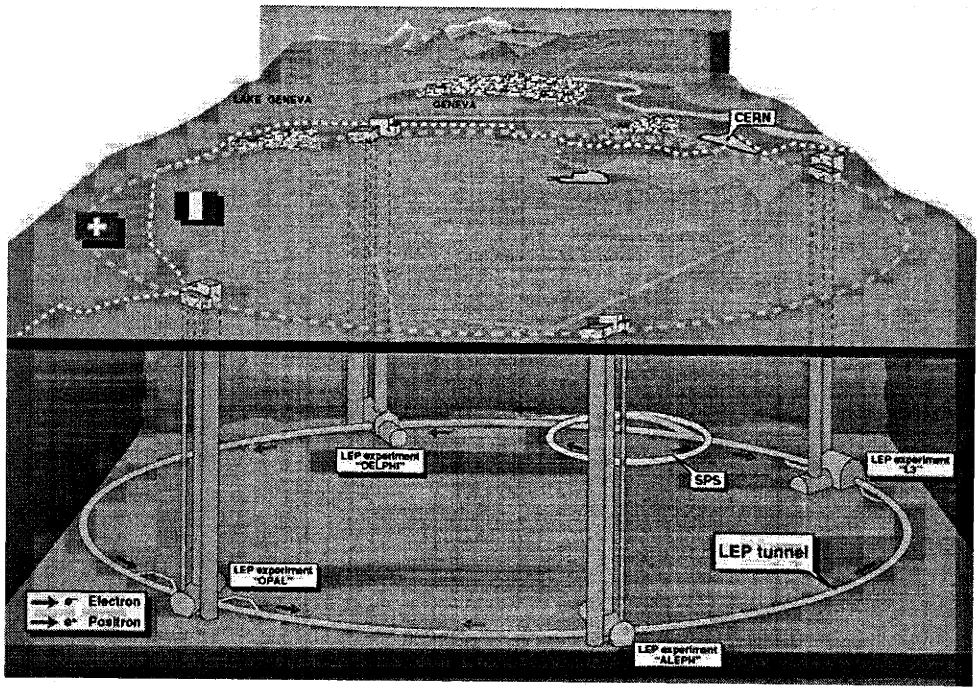

Figure 2-1: CERN and the LEP collider. The four experimental sites, at depths of about 60 to 100 m, and the LEP and SPS are shown.

Coordinate System and Terminology

The following coordinate systems are frequently referred to when discussing detector components and measured event variables: Cartesian coordinates are defined with the z-direction being parallel to the direction of the incoming electron beam, and the x-direction perpendicular to the plane of the beam and pointing upwards, and the y-direction pointing towards the centre of the LEP ring. Cylindrical coordinates, which reflect the barrel-like symmetry of the detector design, are also defined, with the z coordinate defined as above and r and ϕ representing to the radial and azimuthal coordinates. Similarly, polar coordinates are also used with r and ϕ, and the polar angle θ defined such that $\theta = 0$ corresponds to the $+z$ direction. The detector has the general form of a 'barrel' filled with concentric layers, roughly covering the region $\pi/4 < \theta < 3\pi/4$, plugged by 'endcaps', at $\theta < \pi/4$ and $\theta > 3\pi/4$.

Detector Structure

The main characteristic feature of L3 is the ability to measure lepton and photon energies, momenta and directions well by enclosing the whole detector, including the muon chambers, in a solonoidal magnet providing a 0.5 Tesla axial field and employing a crystal electromagnetic calorimeter with high granularity and energy resolution. The subdetectors form radially symmetric layers around the beam pipe and can be separated into tracking detectors and calorimetric detectors. The names and roles of the main subdetectors are listed in Table 2.3, and details of their structure, construction and performance can be found in the references. In addition to those listed, there are many other components, with roles such as the detection of particles with trajectories at lower polar angles, particle time-of-flight measurement, hermeticity augmentation, and the monitoring of the luminosity delivered to L3.

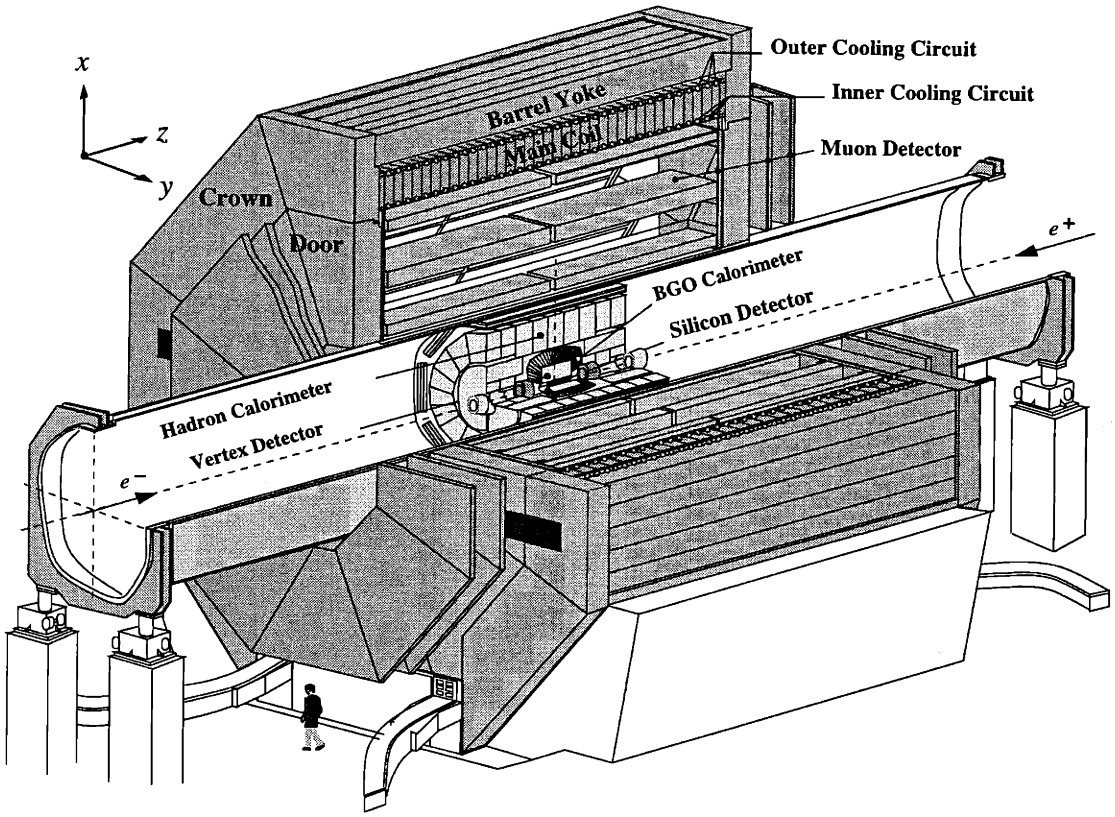

Figure 2-2: The L3 detector.

2.3 Particle Identification and Measurement

Since its inception, methods have been devised at L3 to optimise the use of information from the various subdetectors to identify particles and jets and measure their flight directions and energies and momenta.

Charged particles leave tracks in the central tracking TEC, which has a single wire precision of 50–60μm, with each particle traversing up to 62 wires, and double track separation of 500μm. Transverse momentum measurement precision is $\Delta p_t/p_t \approx 1.8\%$. More precise position information close to the beam interaction point is provided by the SMD, at 5–7 cm from the interaction point, with a spatial precision of 10μm and 15μm in the $r\phi$ and z coordinates respectively. Measurements from the SMD help double the momentum measurement precision. Particle identification is performed using additional information from the other detectors as described below.

Photons and electrons form clusters of energy in the ECAL, which consists of 10752 crystals of bismuth germanate oxide, which has a Moliere radius of 2.4 cm, and a radiation length of 1.12 cm. The crystals are 24 cm in length and have a cross section of 2 to 3 centimetres square. These particles can be distinguished from hadrons since their energy deposits in the ECAL are more localised; the ratio between the energies contained in the central 3 $\times$ 3 crystals and that contained in the central 5 $\times$ 5 crystals is an effective discriminating quantity. A ratio of 0.96 would be a typical value at which to discriminate between hadronic and electromagnetic deposits. The angular distance between such a deposit and the nearest track in the central tracker can then be used to differentiate between electrons and photons. The energy resolution of the calorimeter is $2\%/\sqrt{E(\text{ GeV})} + 1\%$,

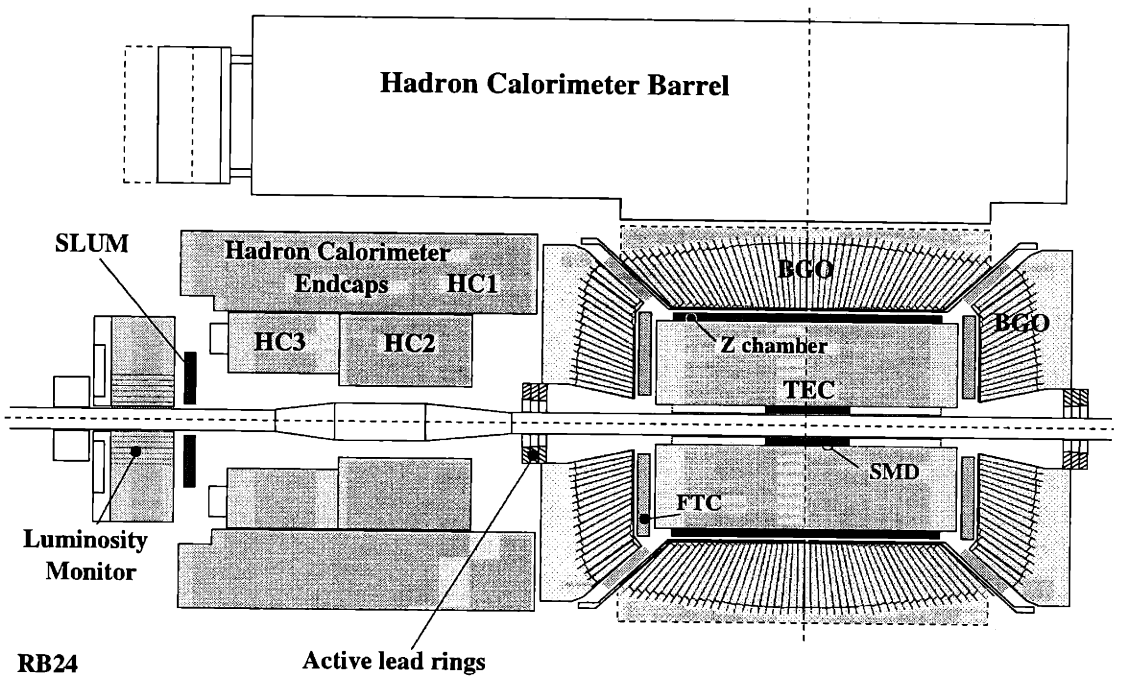

Figure 2-3: Cross-sectional side view of the central section of the L3 detector. The actual detector is symmetric about the dashed lines.

and the angular resolution is 2°, and coverage is $|\cos\theta| < 0.74$ and $0.79 < |\cos\theta| < 0.98$.

Only muons leave tracks in the MUCH and FBMU, and scintillator time information and central track and calorimeter energy deposit matching are used to remove cosmic ray muons, which are the main source of background for events with only muons. The MUCH provide measurements of 54μm and 250μm in each layer for $r\phi$ and z coordinates respectively. The momentum resolution for well reconstructed muons of 45 GeV is about 2.5%. The FBMU can measure muons down to $|\cos\theta| < 0.94$. The muon, being a minimum ionising particle, leaves a characteristically small energy deposit in the calorimeters, and this allows the recovery of isolated muons which do not traverse the active regions of the muon chambers. The use of this signature to identify muons results in an acceptance which is approximately 10% larger than the MUCH and FBMU by themselves.

Since taus decay into one or three charged particles and some neutral hadrons and neutrinos, with branching fractions of 85% and 15% respectively, the tracks and energy deposits they form have a distinctive signature which allows these leptons to be identified.

Tracks and calorimeter deposits which do not fall into the above categories are considered as belonging to charged or neutral hadrons. The energies of these particles, while measured mainly by the HCAL, are calculated by combining contributions from the subdetectors using factors which are found using calibration Z peak running. The calorimeter has an energy resolution of $\Delta E/E \approx 55\%/\sqrt{E(\text{ GeV})} + 5\%$, and an angular coverage of $|\cos\theta| < 0.995$. Many algorithms exist to add the track momenta of these particles together, with the aim being to construct *jets* which reflect the qualities of the underlying particle which generated the observed particles through hadronisation. Of these, the Durham algorithm [46] has been shown to provide a jet energy and direction which satisfies these criteria well and is commonly used. The Jade algorithm [47] is also used here.

The operating status of the detector is consistently monitored and recorded during data taking. Events are labelled in terms of data taking run number and event number, and runs are tagged ac-

Tracking Detectors	Microvertex Detector [40]	Silicon Microstrips (SMD)
	Vertex Detector [41]	Time Expansion Chamber (TEC) Wire Chamber (Z-Chamber)
	Muon Chambers [42,43]	Barrel Drift Chambers (MUCH) Forward-Backward Drift Chambers (FBMU)
Calorimetric Detectors	Electromagnetic Calorimeter [44]	BGO Crystal Matrix (BGO)
	Hadron Calorimeter [45]	Uranium-Gas Proportional Chambers (HCAL)

Table 2.3: Principal components of the L3 detector. Important characteristics of the subdetectors are given in Section 2.3.

cording to the status of the detector. All Monte Carlo (MC) events are given run numbers which are mapped out to correspond to the luminosity recorded in each data run, and the actual detector status for that run is recreated in the detector setup used by the software to simulate the detector response. This allows the variation of detector performance to be reflected in the final event observable distributions.

Runs for which components of the detector which significantly affect this analysis are known to not have been working adequately are removed from consideration in both the data and the corresponding MC. The requirements for a run to be accepted are that the central tracker, scintillators and the calorimeters are functioning correctly.

Chapter 3 — W Boson Production and Observation at LEP II

While the bulk of the physics analysis effort at LEP I concentrated on understanding the production and decay of the Z boson, at LEP II, the W boson has taken centre stage. Both theoretically and experimentally, the investigation of W production events has its own characteristic issues which must be taken into consideration and these will be discussed in this chapter. More specific details regarding the computer programs and experimental cuts mentioned here can be found in the Appendices.

3.1 W-pair Production

Since 1996, when the centre-of-mass energy of LEP first exceeded the W boson pair production threshold of twice M_{W}, this process has been used to measure the W boson mass [48] and production and decay cross sections [49] with great accuracy. The theoretical aspects of this process which are most relevant here are summarised in this section.

W-pair production occurs, at tree-level, through the three charged-current diagrams ('CC03' diagrams) in Fig. 3-1, The non-Abelian structure of the underlying $\mathrm{SU}(2)\times\mathrm{U}(1)$ gauge group manifests itself in the gauge boson vertices in the s-channel diagrams.

Many programs exist which calculate W-pair production cross sections and generate simulated events. Here, events generated by KORALW [50] have been used as the baseline sample for the underlying processes, and JETSET [51] used for hadronisation. The SM prediction for W-pair production at LEP II as calculated using the semi-analytical program GENTLE [52], and L3 data are shown in Fig. 3-2 [53]. From an experimental viewpoint, W bosons decay either into two quarks, which appear as two hadronic jets in the detector, or a charged lepton and an undetected neutrino, with

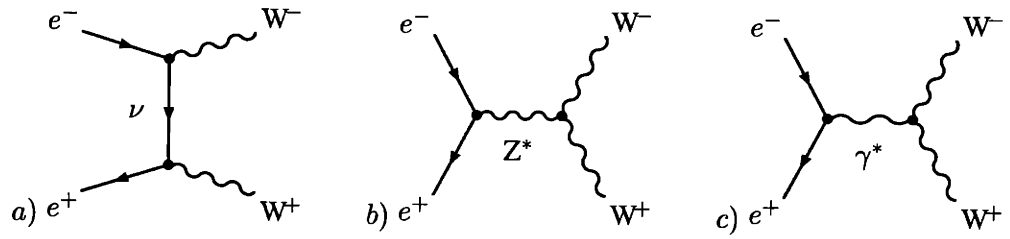

Figure 3-1: The three 'CC03' diagrams that contribute to W-pairproduction events at tree level, *a*) the t-channel neutrino exchange diagram, and *b*), *c*) the s-channel Z and photon diagrams, respectively.

branching ratios [17] of $68.7 \pm 0.9\%$ into hadrons and $10.51 \pm 0.24\%$ into each of the three leptons $e^{\pm}$, $\mu^{\pm}$, $\tau^{\pm}$ and their neutrinos. Therefore, W-pair events present themselves in one of three general topologies depending on the combination of hadronic and leptonic decays which occur. Here, the fully-hadronic and fully-leptonic channels utilise the standard L3 W-Group selections [49], whereas customised selections are used for the semi-leptonic and the single-W [54,55] channels.

Semi-Leptonic Channel ($qq\ell\nu$)
The semi-leptonic channel has the distinctive signature of two jets with the invariant mass properties of W-decay quark jets, and a charged lepton, for which a cut requiring isolation of the lepton from the jets can be used with little loss of selection efficiency. The W boson has a mass and width of 80.396 ± 0.061 and 2.06 ± 0.05 GeV [17] respectively, so the invariant mass of the two jets that a W boson has decayed into remains close to the value of the boson mass. This mass can be measured by the calorimeters to about ± 7 GeV. The charge of the lepton is much easier to measure than with hadronic jets and despite the fact that the neutrino remains unmeasured, the total event kinematics can be reconstructed, up to some ambiguity caused by initial state radiation (ISR), and the extraction of a large amount of information regarding the underlying processes is possible. 43.3% of events belong to this group. Since $\tau^{\pm}$ particles can decay into low energy e's and μ's as well as hadronically, there is an overlap of events between the $qq\tau\nu$ sub-channel and the $qqe\nu$, $qqe\nu$ sub-channels. For the purposes of this analysis, the distinction between these sub-channels is not critical and no attempt is made to separate events between these categories, and both possibilities are considered when estimating the resolutions on the reconstructed leptons when they are introduced to the equal mass (two-constraint [25,48]) kinematic fit to improve the resolution on the measured quantities. The main background is from hadronic Z decays with a radiated photon which is mis-identified as an electron due to a nearby charged particle track, or with isolated muons from semi-leptonic heavy quark decay, or which have a third low energy gluon jet.

Fully-Hadronic Channel ($qqqq$)
The fully-hadronic channel has an evenly balanced four jet topology, with little missing energy. About 47.2% of W-pair events fall into this category. Since the flavours of the original decay quarks are difficult to reconstruct, there is some ambiguity in the assignment of jet pairs to the W particles from which they originate. A kinematic fit is performed with equality constraints on the invariant masses of the paired jets (five-constraint). The constraints imposed are four momentum conservation, and equality between the two reconstructed W masses. 2/3-jet events from non-resonant γ/Z^*-exchange QCD processes form the dominant background, while at the high energies analysed here, Z pair production with hadronic decays is a process with a relatively low cross section but an event signature similar to that of the signal process.

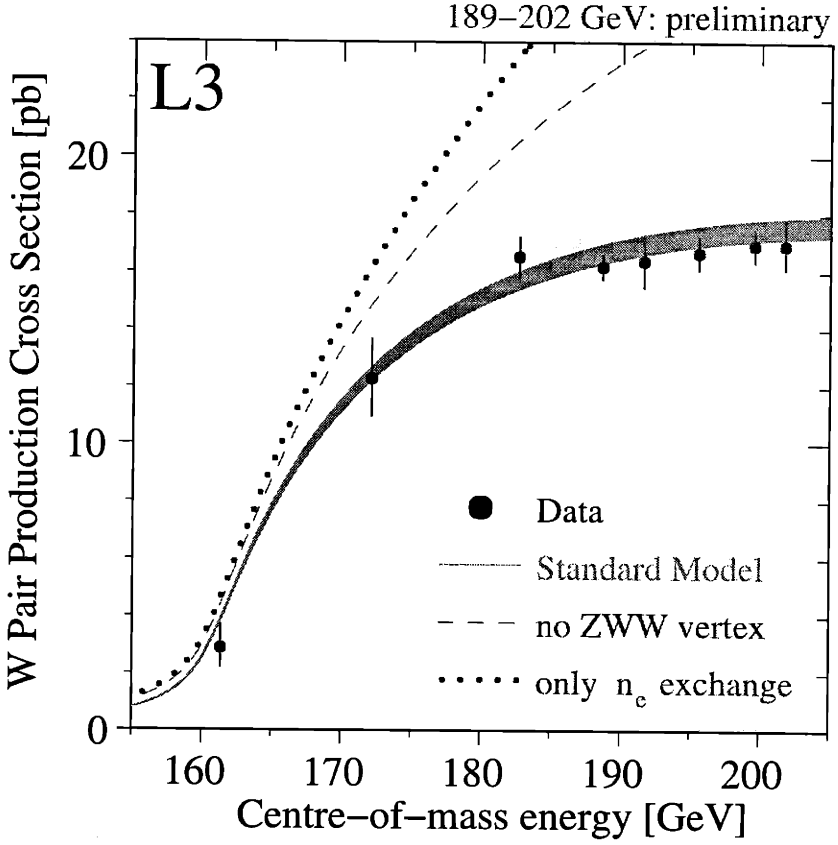

Figure 3-2: The W-pair production cross section as a function of LEP centre-of-mass energy [53]. The band shows the SM expectation and the points are for L3 data, with those corresponding to 189 GeV and above being preliminary.

Fully-Leptonic Channel ($\ell\nu\ell\nu$)

Of all W-pair production events, 9.9% have two charged leptons, and a large amount of missing energy corresponding to the two neutrinos from each of the decaying bosons. The missing information regarding the neutrino momenta leads to a two-fold ambiguity in the reconstruction of the original W production parameters, while the charges of the leptons can be identified with very little ambiguity. Low particle multiplicity processes such as Bhabha scattering, di-lepton production and two photon events form the main background.

3.2 Single-W Production

While the investigation of W-pair production was one of the main physics goals leading to the high energy running phase of LEP II, with the collision energies specifically chosen to be optimal for their observation and a significant amount of effort going into their study prior to LEP II, the significance of single-W production events in providing gauge sector information was brought to attention during the early days of LEP II running [56]. The expression 'single-W production' [57] refers to events in which an on-shell W boson is produced with one of the beam particles being barely deflected and disappearing down the beam pipe. The process is a background for the Higgs boson search in the $e^{\pm} \rightarrow H\nu\bar{\nu}$ channel. The final state particles for such a process are identical to those for W-pair production processes which include a final state electron or positron, but unlike the latter processes, the 'CC03' diagrams are not sufficient for calculating the amplitudes for the single-W processes.

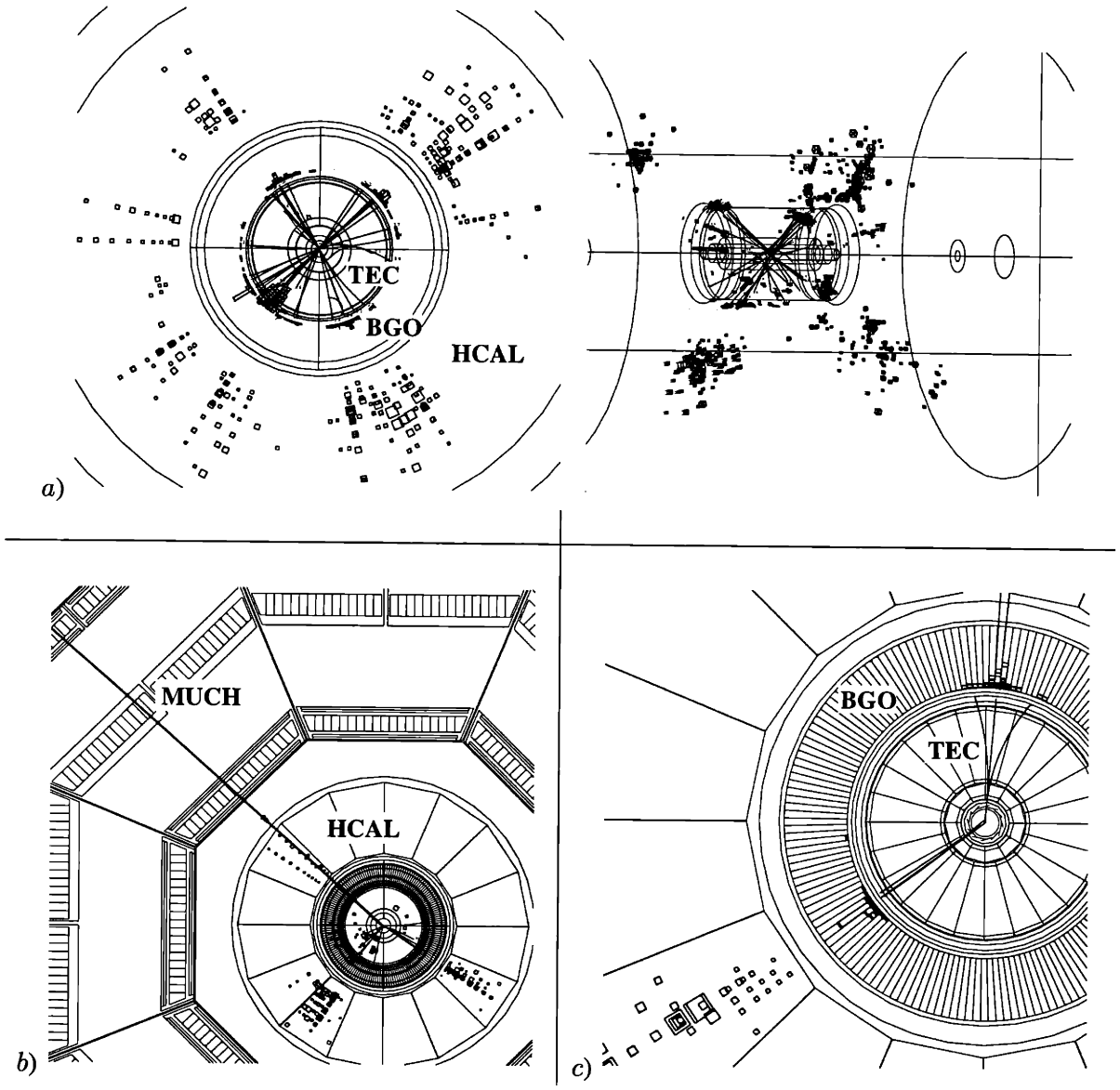

Figure 3-3: Examples of *a*) $qqqq$, *b*) $qq\mu\nu$ and *c*) $\tau\nu\tau\nu$ event candidates seen by the L3 detector. In *a*), longitudinal and transverse views of the same $qqqq$ event are shown, both in a simplified schematic of the detector. Four distinct jets are clearly visible in the Time Expansion Chamber, as are their energy deposits in the BGO electromagnetic calorimeter and the Hadronic calorimeter. The events in *b*) and *c*) are shown with a more detailed rendering of the detector components. Two jets are visible in *b*), while a muon is observed as a track in the central tracker, small characteristic energy deposits in the calorimeters, and as hits in all three layers of the barrel muon chambers. Two three-prong τ jets are visible in *c*). There were no other significant tracks or energy deposits in either event.

Twenty diagrams contribute to final states with one electron or positron and its neutrino, and fifty-six diagrams exist for $e\nu e\nu$ final states (cf. Appendix B). This kinematical configuration results in a category of events where the t-channel γ-W interaction dominates, allowing this specific aspect of gauge boson couplings to be probed relatively independently of the other aspects, in contrast to the W-pair production processes of Fig. 3-1, where the Z and γ contributions cannot be distinguished. In terms of the couplings defined in Section 1.3, κ_γ and λ_γ are singled out by this corner of phase space. The single-resonant nature of the process is evident in Fig. 3-4.

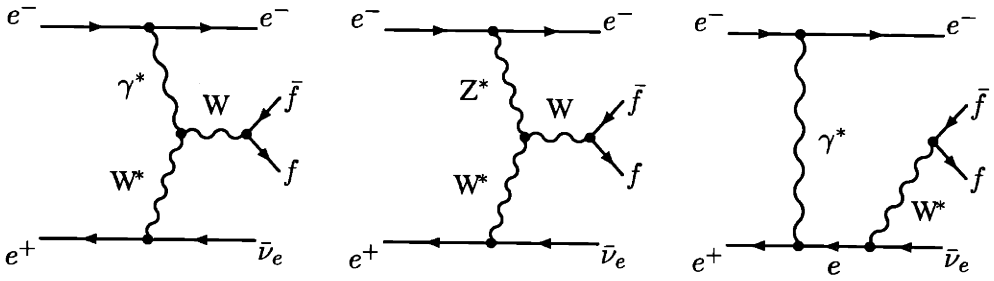

Figure 3-4: Examples of single-resonant t-channel diagrams. The first diagram dominates over the second due to the large mass of the Z boson, hence the sensitivity of this process to the W-γ vertex. The full set of 'CC20' diagrams can be found in the Appendix B.

For this analysis the following definition for the single-W signal is used:

$$|\cos(\theta_{(e^{\pm})})| > 0.997 \quad E_f, E_{\bar{f}} > 15 \text{ GeV} \tag{3.1}$$

for the polar angle of the electron lost in the beam pipe, and the energies of the two fermions other than this electron and its accompanying neutrino. For the single resonant processes, these fermions constitute the $W^{\pm}$ decay system. These requirements apply to the four fermions emerging from the interactions point, ie, 'generator level' particles. The two fermions $f\bar{f}$ can be quark pairs, or a charged lepton and its corresponding neutrino. For the case where the charged lepton is an $e^{\mp}$, the condition

$$|\cos(\theta_{e^{\mp}})| \; < \; 0.75 \tag{3.2}$$

is imposed on the visible electron because of the large number of background events from low track multiplicity processes which have low angle electrons, such as Bhabha scattering, Compton scattering and processes with photon conversion into an electron-positron pair.

The signal definition is not unique among experiments, and is to be standardised in the near future to allow the comparison and combination of results; the cross sections values obtained using the above definition should be related to that from any other definition by a simple conversion factor.

The complications inherent in the calculation of the amplitudes for this process imply that many programs are excluded from being used for this region of phase space [58,59]. One of the difficulties is due to the huge gauge cancellations which occur between diagrams, and the existence of a resonant heavy boson. The main diagrams involved at tree level, when their amplitudes are squared individually, contribute cross sections of $\mathcal{O}(10^5)$pb , while their combined contribution is $\mathcal{O}(0.1)$, with the cancellations occurring in the region where the electron deflection is less than 50 mrad. When resonant W's are involved in other regions of phase space, the substitution $(q^2 - M_W^2)^2 \to (q^2 - M_W^2)^2 + M_W^2\Gamma_W^2$ in the amplitude calculated in the zero width limit generally suffices as a way of obtaining a stable approximation to the true value. This procedure is actually equivalent to introducing just those higher order diagrams which contribute to the effect of the width of the boson, but since gauge cancellations occur order-by-order, they are rendered incomplete after this naive method of introducing the width effects, and the calculation becomes completely unreliable. The cross section for this process also diverges in the limit $M_e \to 0$, and the many programs which employ the massless approximation for all fermions cannot be used.

The production of new programs capable of overcoming these difficulties is a currently active field. Here, the programs EXCALIBUR and GRC4F have primarily been used to provide calculations for this process (cf. Appendix C.3). The former program is used with a minor modification to

overcome the problems caused by the massless fermion approximation used by the standard version, and the latter retains all fermion masses in the calculations and uses the 'preserved gauge method' [58] to maintain gauge invariance.

In terms of experimental signature, single-W events are similar to $qq\ell\nu$ and $\ell\nu\ell\nu$ events, with the difference being the absence of one visible charged lepton. For the hadronic channel, the lack of the distinctive charge lepton implies that the background conditions are subsequently harsher. Here the similarities between the channels are utilised to allow a common set of cuts to be applied in selections for both event categories. Leptonic single-W events simply have one visible charged lepton. Excess energy in the low angle calorimeters and energy deposits not belonging to a narrow cone around the lepton candidate are cut upon to reduce background from two fermion events with a badly reconstructed second fermion. A lower bound on the lepton energy is introduced to remove low energy electrons from two-photon and $Zee \to \nu\bar{\nu}ee$ events.

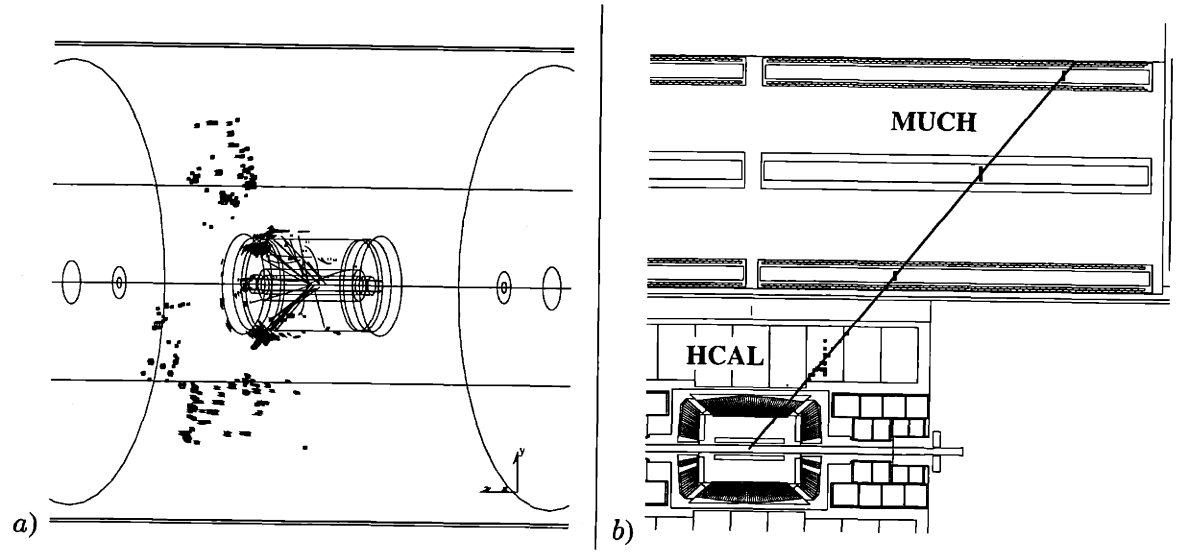

Figure 3-5: Examples of *a*) hadronic and *b*) muonic single-W event candidates seen in the L3 detector. The hadronic event is shown with energy deposits and tracks superimposed on a simplified schematic of the detector, while the detector components are shown in a partial transverse view for the leptonic events.

3.3 Event Selection

The aim of the selection procedure is to provide the fitting algorithm with event samples, categorised according to the well reconstructed event elements found in the events, which have a high proportion of events which are sensitive to the parameters to be measured. As can be seen to follow from the descriptions of the signal processes in the previous chapters, the event groupings can be summarised as follows:

For the $4j$ and 2ℓ categories, the selection requirements are shared with the standard selections [49] for cross section measurements, and therefore these selections are used as the starting point here.

A customised selection is employed for the $2j$ and $2j1\ell$ categories, which concentrates on the requirements of coupling measurements and cross section measurements in the single-W channel. Less emphasis in placed on the distinction between lepton categories. The $2j$ category contains as many as possible of the hadronic single-W events, and the $qq\ell\nu$ events with badly reconstructed leptons, since both of these are sensitive to the couplings, while the coupling insensitive background is minimised. Within the $2j$ category, as much information regarding the difference between events

Reconstructed Quantities	Primary Sensitive Signal
2 jets & 1 lepton	WW$\rightarrow$ $qq\ell\nu$
2 jets†	a) WW$\rightarrow$ $qq\ell\nu$ with badly reconstructed lepton
	b) W(e)ν $\rightarrow$ $qq(e)\nu$
4 jets	WW$\rightarrow$ $qqqq$
2 leptons	WW$\rightarrow$ $\ell\nu\ell\nu$
1 lepton	W(e)ν $\rightarrow$ $\ell\nu(e)\nu$

Table 3.1: Event reconstruction categories and their correspondence with the signal categories.. The symbol '(e)' refers to unobserved extremely low polar angle electrons in single-W events. †The $2j$ category is parametrised using a neural network into events likely to be from genuine hadronic single-W production, and those from $qq\ell\nu$ with a badly reconstructed lepton.

from genuine hadronic single-W and $qq\ell\nu$ W-pair events is to be incorporated into the parameter extraction.

To meet these needs, a set of basic selection cuts is set up with the hadronic decay of one W boson as the target 'signal'. Specific cut details can be found in Appendix C.1. Each event is passed through these cuts several times depending on the number of identified leptons. The first pass is made with the full event reconstruction, then for each lepton that is identified in the event, a new pass is made after reconstructing the event with all elements related to the identified lepton removed. If the identified lepton is a W-decay lepton from a $qq\ell\nu$ event, the rest of the event should pass the selection criteria for one hadronic W-decay, so if an event passes the selection at this stage, the lepton is considered a candidate as a W-decay lepton. This step is repeated for each lepton that is identified in the event. If more than one lepton remains as a W-decay candidate, the one with the highest probability as being such, when the event is processed in a kinematic fit for $qq\ell\nu$ events with the candidate lepton and the two jets as input, is chosen as the best candidate.

Following this procedure, the events that remain all have two reconstructed jets, and possibly a W-decay candidate lepton. The next step is to separate these into several categories; a) events which are likely to be coupling sensitive W-events but which do not have a reliable lepton because they are either a') $qq(e)\nu$ events or a'') $qq\ell\nu$ events with badly reconstructed leptons, b) those for which the lepton is likely to be a well reconstructed W-decay lepton, and finally c) coupling insensitive background events.

Two artificial neural networks are used for this purpose, which are implemented using JETNET [60]. The first, to be denoted NNET I, is used on events which do not have an identified lepton. Its has two output nodes which can each take values within the range $[0,1]$ in the form (x_1^{outI}, x_2^{outI}). NNET I is trained to produce the output $(1,0)$ for $qq\ell\nu$ and $(0,1)$ for $qq(e)\nu$ events and $(0,0)$ for background events. A second network, NNET II, with a single output node x^{outII}, is used for events with an identified lepton, and is trained to output 1 for $qq\ell\nu$ events, and 0 for all other events. Some input variables distributions for the neural networks are shown in Fig. C-1. For details see Appendix C.1. The property of neural network output values that they represent the conditional probabilities of the desired outputs being one [61], if appropriate training methods are used, allow these output values to be interpreted as likelihoods for the events to satisfy the signal criteria for the category.

An example of the neural network event discriminator output for semi-leptonic W-pair events with reconstructed leptons is shown in Fig. 5-1. Full numerical results can be found in Chapter 5. The NNET II network is used on events for which a candidate lepton has been identified, and then such events which also satisfies the original invariant mass upper limit cut are also processed using

NNET I, and the event is given the value $(1 - x^{outII}) \times x_i^{outI}$ as its modified NNET I output. This allows events where the lepton cannot be correctly reconstructed, but which nevertheless possess a lepton candidate, to be selected as a $2j$ reconstructed $qq\ell\nu$ event. About 5% of $qq\ell\nu$ events fall into this category. Events without candidate leptons have only their NNET I values calculated.

For more specific details of the selection algorithm for the $2j1\ell$ and $2j$ categories, cf. Appendix C.1.

The 1ℓ category has a small number of events, and each event has only energy, charge and polar angle information for the single lepton, and therefore a less sophisticated approach is taken, where events which are accepted by the selection are compared without any additional weighting. The lepton flavour is significant in terms of understanding the contributions of the underlying diagrams for this process, and is taken into account when evaluating the couplings.

Chapter 4 — Extraction of Physical Parameters

The information that has been distilled from the events by the reconstruction and selection procedure can now be used to extract the values of the triple gauge couplings which provide the best description of the data. Both the production cross sections of W events and the distributions of event shape variables are used for this purpose. The constraints from the two sources of information are combined to provide the final results. In this chapter, the method used to simulate the effects of varying the underlying parameter values is first described, followed by the specifics of the two types of parameter extraction.

The method by which the data and MC are combined to obtain an expression to be minimised is shown in Fig. 4-1. The expression for the χ^2, which will be described in detail in the following sections, can be written

$$\chi^2_{\text{total}}(\Phi) = \sum_{\left(\substack{\text{c.m.}\\ \text{energies}}\right)} \Bigg(\chi^2\Bigg(\sum_{\text{cat}\in\binom{4j,\,2j1\ell,}{2j\text{-}a),\,2\ell)}} \sum_{i\in\text{MC}_{\text{cat}}} \omega_i(\Phi)\cdot p_i^{\text{cat}},\ \sum_{\text{cat}\in\binom{4j,\,2j1\ell,}{2j\text{-}a),\,2\ell)}} \sum_{i\in\text{data}_{\text{cat}}} \omega_i(\Phi)\cdot p_i^{\text{cat}}\Bigg) \tag{4.1a}$$

$$+ \sum_{\text{cat}\in\binom{4j,\,2j1\ell,}{2j\text{-}a),\,2\ell)}} \Bigg[\sum_{i\in\text{data}_{\text{cat}}} \chi^2\Big(\sigma_i^{\text{MC}}(\Phi), \sigma_{\text{cat}}^{\text{MC}}(\Phi)/N_{\text{data}}\Big)\cdot p_i^{\text{cat}}\Bigg] \tag{4.1b}$$

$$+ \sum_{\text{cat}\in(2jb,\,1\ell)} \Bigg[\sum_{i\in\text{data}_{\text{cat}}} \chi^2\Big(\sigma_i^{\text{MC}}(\Phi), 1\Big)\cdot p_i^{\text{cat}}\Bigg]\Bigg), \tag{4.1c}$$

where Φ represents the set of couplings values for which the χ^2 is being evaluated, the event categories refer to those listed in Table 3.1, p_i^{cat} is the weighting parameter for MC and data events for each W-pair category, ω_i is the coupling dependent weight for each MC event, normalised to the integrated luminosity for the corresponding data taking period, σ_i^{MC} is the clustered MC event cross section around each data event i. The expression $\chi^2(y, F)$ represents a standard least-squares χ^2 term for mean F and measured value y, with the implied use of the appropriate variances.

4.1 Monte Carlo Samples and Coupling Dependency Modelling

The method described in Section 3.3 results in the event category groupings of Table. 3.1, with samples of MC events and data events belonging to each. The MC sample distributions must now be varied as a function of the parameters and then compared with the data. The starting point is a large sample of events generated for all relevant signal and background processes, with the input parameters set to their standard model values. Each simulated event has assigned to it a weight,

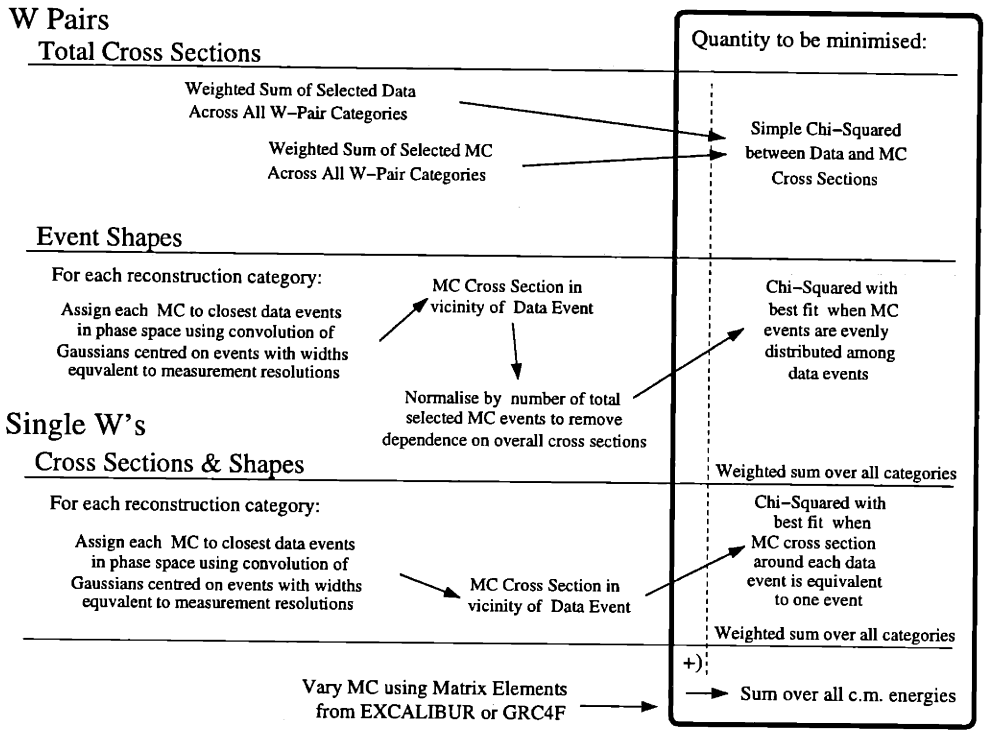

Figure 4-1: Overview of fitting procedure.

which is the number of events of the same underlying process it would correspond to in the data; this depends upon the number of simulated events of the same category that have been generated, the cross section of the process simulated in that category and the total amount of data actually collected. This weight is calculated according to SM predictions. Each simulated event is also accompanied by a set of four vectors describing the particles emerging from the core process before hadronisation and detector effects are introduced. By taking this information, and feeding it into a program which can calculate the effective matrix elements, the relative weight change compared to the SM weight can be found, and by using this new weight for the event, a new distribution of events generated phase space can be produced, which reflects the changes in the input parameter values. This new distribution can then be compared with the data.

Matrix Element Calculations

The programs GRC4F and EXCALIBUR (cf. Appendix C.3) are employed to generate the dependency of MC event weights on variations in the underlying gauge boson couplings. The programs themselves, in their original forms, are designed to be used to calculate cross sections and to generate MC events, and therefore the parts of the codes which calculate the matrix elements are extracted and used here. The two programs possess slightly different sets of variable couplings, namely the six couplings of Eq. 1.18 which are not parity or charge conjugation violating for GRC4F, and the five couplings of Eq. A.1 and an additional parity violating coupling z_z for EXCALIBUR. The couplings used by the latter program can be written in terms of the couplings of Section 1.3, and the sets partially overlap as subsets of the full set of possible couplings in the Lagrangian of Eq. 1.16. These are used to verify that the coupling dependencies of the weights are numerically equivalent between the two programs, which results in an agreement of within 1%. The difference is taken into account as a systematic error, while the program to be used to evaluate the couplings is chosen

depending on the set of couplings which are to be left free to vary in the particular fit which is being undertaken.

4.2 Constraints from W-pair Production Cross Sections

The coupling values at the three boson vertices directly affect the total production rate of W-pair and single-W events. For the W-pair cross section, a weighted sum of events observed across all W-pair event categories is calculated for each collision centre-of-mass energy. The weighting is used to ensure that double counting does not occur for events which are selected in more than one category. The equivalent quantity is calculated for the MC samples, which can be reweighted as described in the previous section. This provides the cross section of MC events accepted by the selection, as a function of the couplings as desired. The error of this quantity is calculated at the same time, and these are combined into a single χ^2 term for the coupling constraints from the W-pair cross section (Eq. 4.1a). The event categories which are combined for this are the $4j$, $2j1\ell$, 2ℓ, and $2j$-a, the $2j$ sample with high $qq\ell\nu$ likelihood.

The single-W channels are treated differently due to the fact that the different decay modes are dominated by different underlying diagrams, and the efficiencies and background characteristics vary greatly between channels. The combination of cross sections across the different reconstruction categories has less meaning in this case, and a single fit using both shape and absolute cross section information is performed and is described later in this chapter.

4.3 Constraints from Event Shape Distributions

The strategy for using the event shape variable distributions is to take the collections of selected MC and data events in each category, and compare their distribution in phase space. A clustering method is employed, which assigns each MC event to the data events which are in its vicinity in phase space. The method takes into account the measurement resolutions of the quantities which are represented in phase space, which reduces the jitter in the assignment procedure due to limited MC statistics, while maintaining at a minimum the loss of information caused by the fitting procedure. The details of the method are described here, while specific numerical information is summarised alongside the results in the following chapter.

Event Comparison Variables

The observables to be compared between events are chosen to reflect the W boson production kinematics which are sensitive to the values of the underlying couplings, while allowing their resolutions to be computed with relative ease. The choice of straightforward fitting to simple experimental observables allows the investigation of deviations in all calculable couplings without extra optimisation, and is suited to constraintless multidimensional fits to many couplings.

The kinematics of a W-pair event, under the simplifying assumption that it can be considered as two W bosons being produced back-to-back in the rest frame, which decay into two fermions whose identities are known, are fully specified by five characteristic angles: θ_{W^-}, the polar angle of the pair production axis and $\theta^*_{\mathrm{W}^\pm}$ and $\phi^*_{\mathrm{W}^\pm}$, the polar and azimuthal angles of the $\mathrm{W}^\pm$ decay vectors in the rest frames of the $\mathrm{W}^\pm$ particles, with respect to the W-pair production axis and the plane containing this axis and the beam direction. These definitions are shown schematically in Fig. 4-2.

These angles characterise the event shapes, which are sensitive to the underlying couplings, and the distributions of events in the multidimensional phase space described by these quantities are compared to allow the evaluation of the desired coupling values.

A selection of such variables, with comparisons between data and MC, are shown in Fig. 4-3. For experimentally observed events, the final state fermions are not perfectly identified, so best values for these angles must be evaluated using appropriate approximations. The characteristics of

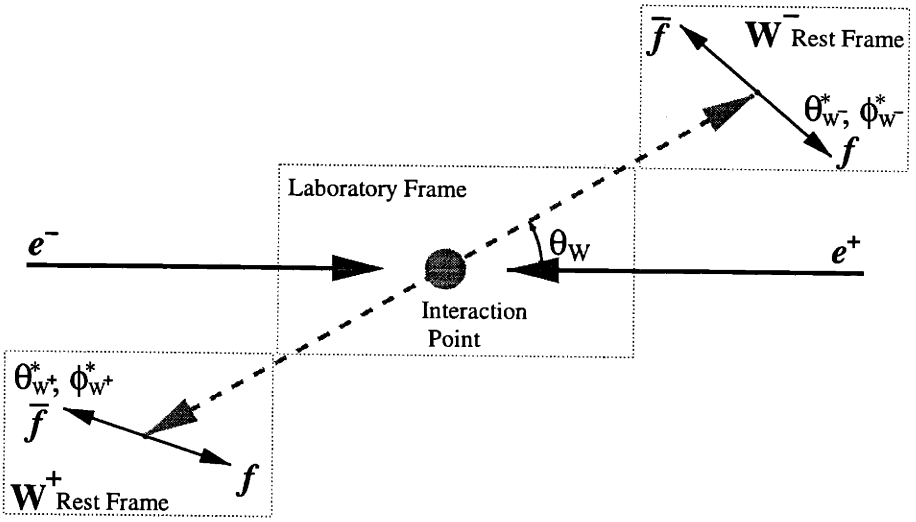

Figure 4-2: The five angles which fully describe W-pair production kinematics at a given collision energy, when the boson pair is assumed to be produced at rest. The angles $\theta^*_{W\pm}$ and $\phi^*_{W\pm}$ represent the $W^\pm$ decay angles in the boson rest frame, in polar coordinates taken around the W-pair production axis, with the azimuthal angle being measured with reference to the plane in which this axis and the beams lie. Complications arise when identifying and measuring the kinematics of the decay fermions which necessitates the use of approximations and weighting when evaluating the quantities.

event reconstruction in each event category are reflected in the way in which this angle information is extracted. The experimental properties of the observable quantities for each decay channel define the methods and uncertainties involved.

For the $4j$ channel, the existence of three possible ways of pairing four reconstructed jets, to be taken as the pairs which result from the decay of the individual W bosons, introduces a large ambiguity. The best pairing is determined with an algorithm which takes the masses of the two W's from a kinematic fit and uses their difference and sum to find the most likely pairing. Approximately 70% of events have the correct pairing with this algorithm. An additional ambiguity exists since the charges of the fermions from which the hadronic jets originate cannot be accurately measured. This affects the directions of the reconstructed W production and decay vectors. Here, a jet charge algorithm is used, which weights the charges of the tracks in the jets by their momenta along the jet axis, to estimate the charge of the mother fermion. The five angles for all jet combinations are calculated, and comparisons for all combinations are made and weighted according to the likelihood of correct charge matching between jets, assuming simple Gaussian distributions of the jet charge measurement error. The WW system charge designation is correct at the 70% level.

Both the charge and momenta of charged leptons are well measured, which reduces the ambiguity present in $2j1\ell$ events to that of the decay vector of the hadronic W. Weighting, similar to that for the $4j$ channels is used here. For 2ℓ events, while the charges and momenta of the leptons are well measured, it can be shown that the two missing neutrinos introduce a purely mathematical two-fold ambiguity in the reconstructed event angles. A simple algorithm can be used to find the two sets of angles given the measured lepton momentum vectors. This is true under the assumptions given above for simple W pair production at rest, however, in practice, the effects of initial state radiation and reconstruction resolutions can skew the measured momenta and angles, rendering the two solutions of the algorithm imaginary for approximately one third of signal events in this category. In this case, a single real solution is found by setting the imaginary part to zero, and this is used as the best estimate of the five angles.

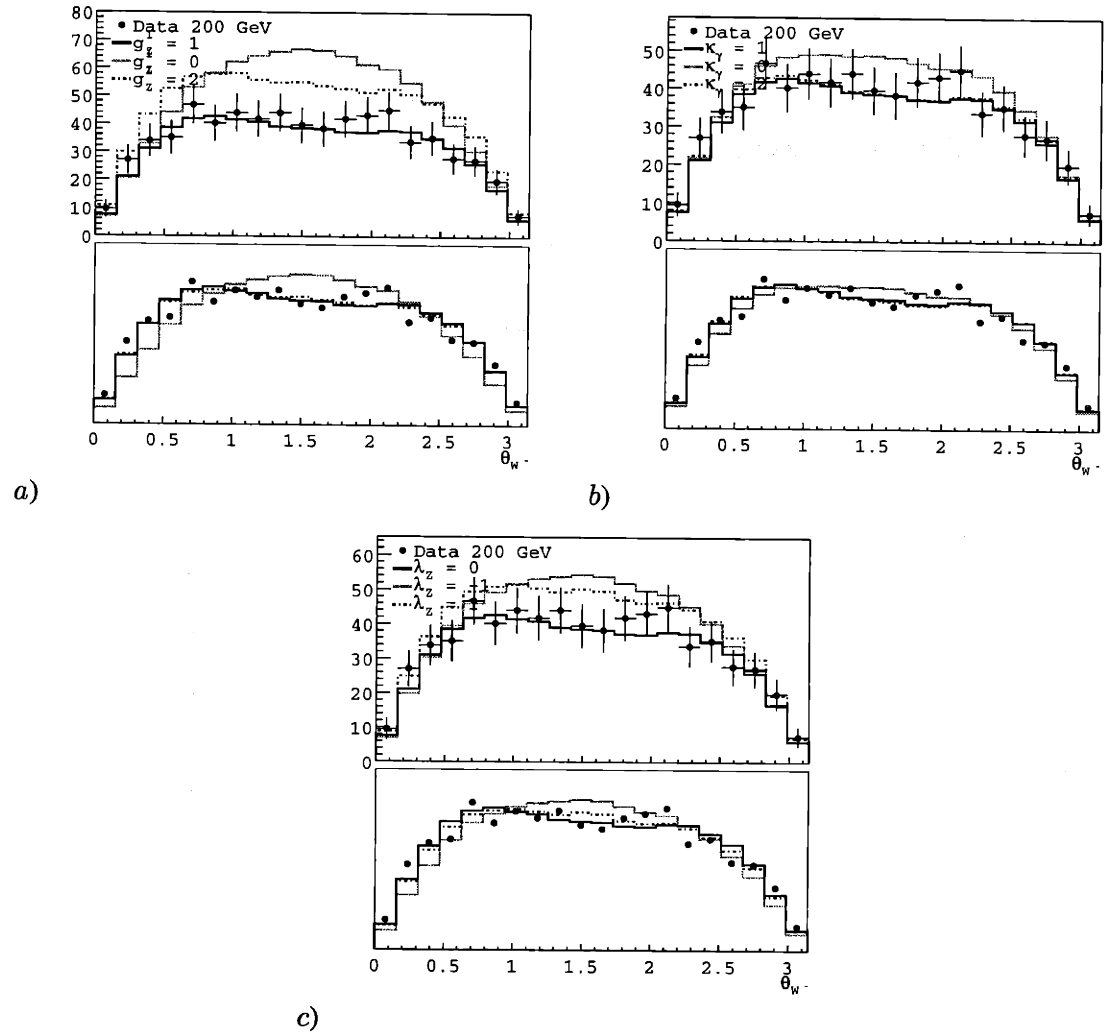

Figure 4-3: A selection of the variables used in the comparison of event distributions between data and MC and their dependence on coupling values. *a*, *b*, *c*) The W production axis polar angle θ_{W^-} for $qqqq$ event, with the three couplings g_1^Z, κ_γ and λ_γ above and below their SM values by unity in the linear realisation model. The distributions shown are for the reconstructed quantities after full detector simulation for the MC, and the actually measured values for the data. The upper plots are of the absolute cross sections and events observed, while the lower plots are normalised to remove the total cross section dependence, and show the change of the shape according to variations in the underlying physics parameters.

Event Distribution Comparisons

A comparison can now be made between the MC and data in each event category. This is performed by first assigning each MC event to data events which are close to them in phase space. For each MC event, Gaussian probability distributions centred around the measured values in phase space are considered, with widths corresponding to the measurement resolutions of the variables, and the convolutions of these Gaussians with similar distributions around each data event are integrated over. This provides a number for each MC and data event pairing corresponding to the degree of overlap between the events in phase space. This quantity is normalised such that the sum of contributions over all data events is unity for each MC event.

As a result of this procedure, each data event has a weighted grouping of MC events in its vicinity assigned to it, and in the limit of perfect agreement between the probability density distributions

of the data and MC, the luminosity normalised MC event multiplicity assigned to each data event would be identical across all data events. This in effect acts as a way of binning [62] the MC sample into groups with the expectation values of the MC in each bin being unity, but with overlapping bin boundaries to counter the adverse effects of low statistics binning in multidimensional space.

The distribution of MC events in these groupings can now be evaluated using a least squares fit, which is combined with the other terms to form the expression for the full χ^2.

4.4 Constraints from Single-W Events

As mentioned above, single-W events are fitted using cross sections and event shape variables simultaneously. The bulk of the useful information originates in the cross section, and the role of the event variables is to further discriminate between the signal and background, taking the place of the explicit weighting of events which is used in the W-pair case.

Only the production and decay angles of one W boson can be obtained in the case of hadronic single-W events, while for leptonic single-W events, only the energy and polar angle of a single lepton is available and the reconstruction of further underlying event parameters is not possible. The distributions of signal and background events are different in these variables and while comparisons of events using these can improve the measurements, the lower cross sections, higher backgrounds and reconstruction ambiguities make the use of pure event shapes difficult. Therefore the a similar procedure is followed to the event shape analysis for the W-pair events, but instead of normalising the MC cross sections attributed to each data event to eliminate the cross section dependency of the χ^2 terms, the absolute values of the cross section predictions are used.

4.5 Systematic and Theoretical Uncertainties

Many sources of systematic and theoretical uncertainties exist which have the potential to introduce biases in measured quantities, and affect the sensitivity of the measurement. Their effect on the results have been estimated.

The sources of uncertainty which have been taken into consideration are the theoretical uncertainties on the WW, ZZ, single-W, and $\gamma\gamma$ interaction cross sections, the matrix element calculations, and the effects of the modelling of Bose-Einstein correlations [63], Colour Reconnection [64], and Fragmentation Algorithms [51,65]. Detector and simulation effects have also been estimated.

The systematic errors on the signal and background cross sections have been the subject of ongoing studies, and the uncertainties used here are obtained from such studies in the case of the WW and single-W cross sections [66], and by comparing MC generators for ZZ, and for the two-photon interactions, a conservative estimate is taken from comparisons with data using samples with enriched background contributions from this process (cf. Appendix C.1).

The uncertainties are evaluated separately for their effect on the particular couplings which are being fitted, and folded into the final numbers, assuming Gaussian distributions and no correlations between the different types of uncertainties, and full correlations between the uncertainties at different collision energies. This is performed by using MC events generated with different values of the sources of uncertainty, and fitting to them as if they were data events. The shifts in obtained values are taken as uncertainties in the measurement, and convoluted into the likelihood distributions of measured quantities after summation in quadrature. This test is not performed at all centre-of-mass energies but at 189 or 200 GeV, and the errors for the other energies are estimated from the results.

For theoretical uncertainties in the cross sections of the background processes, the entire fit with all channels and centre-of-mass energies is performed while varying the input cross sections by their

uncertainties and their effects are incorporated into the final results.

Chapter 5 — Results

The results of the event selections are first summarised. Next, the results of the fits are presented in different ways corresponding to the large range of physics for which the information can be applied. The couplings are often best expressed in the form of likelihood plots, but a numerical summary is provided to facilitate comparison between results.

5.1 Event Selections

Fig. 5-1 shows an example of the distribution of the neural network outputs for the $2j1\ell/2j$ selections, for 202 GeV centre-of-mass energy.

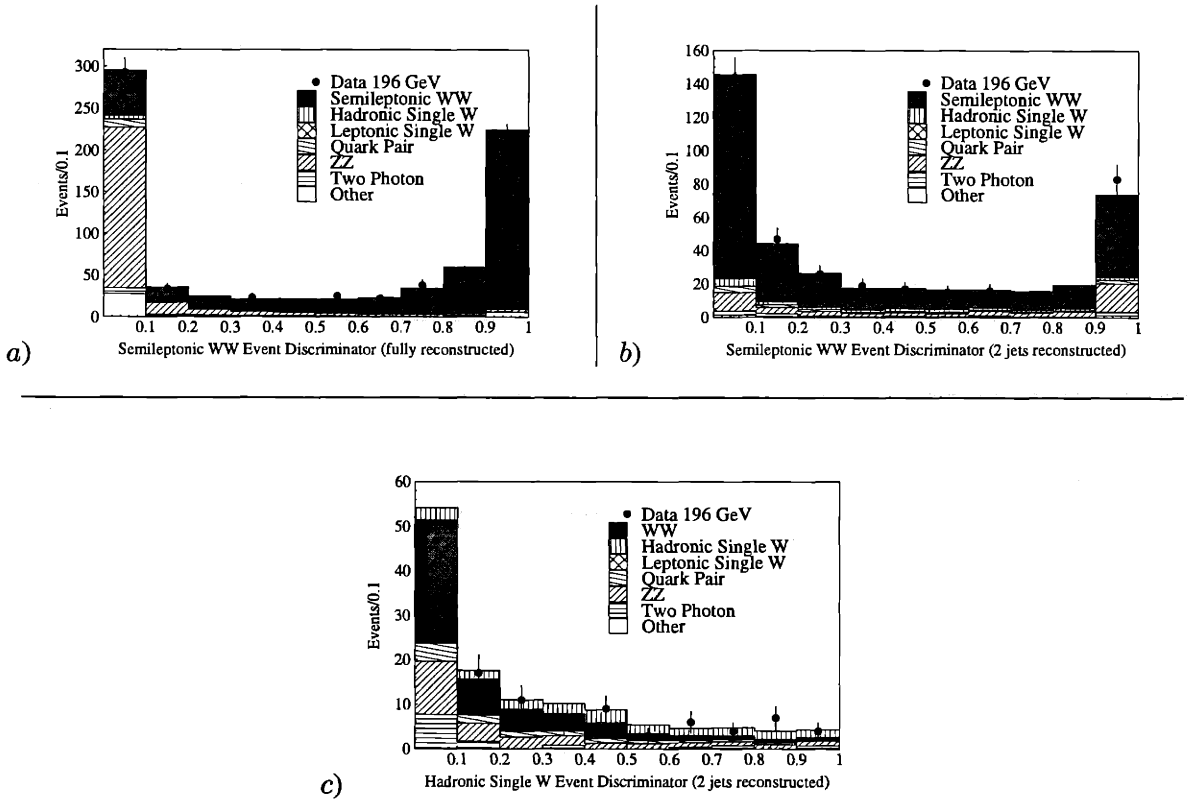

Figure 5-1: The semi-leptonic W-pair and hadronic single-W event selection neural network discriminator outputs for 200 GeV centre-of-mass energy. The MC is normalised to the integrated luminosity corresponding to the data of 82.8 pb^{-1} . Figure *a*) shows events when reconstructed with two jets and a lepton, and the quantities in *b*) and *c*) are calculated with only the two jet hadronic system being reconstructed. In general, individual events can appear in each of the event reconstruction categories. The three plotted quantities for each event have the property that their sum is less than 1.0 by construction, and are used as event weights for fits which are performed within each reconstructed event category.

Tables 5.1 and 5.2 list the number of expected and observed events for the $qq\ell\nu$ and hadronic single-W selections respectively, when the value 0.3 is chosen as the lower threshold for event selection for illustrative purposes.

$E_{\text{c.m.}}$(GeV)	$N^{\text{MC}}_{\text{background}}$	$N^{\text{MC}}_{qq\ell\nu\text{ signal}}$	Efficiency (%)	$N^{\text{MC}}_{\text{total}}$	N_{data}
189	136.3	924.0	74.7	1060.3	**1025**
192	27.5	161.2	76.9	188.7	**196**
196	91.0	456.7	76.2	547.7	**549**
200	71.3	442.3	75.4	513.6	**471**
202	34.8	202.4	75.5	237.2	**253**

Table 5.1: The selection results for semi-leptonic W-pair events, where a lower cut value of 0.3 on the discriminating variables has been chosen for illustrative purposes. For the fitting procedure, close to the full range of events, with discriminating values of 0.05 and above, are used as input.

$E_{\text{c.m.}}$(GeV)	$N^{\text{MC}}_{\text{background}}$	$N^{\text{MC}}_{qq(e)\nu\text{signal}}$	Efficiency (%)	$N^{\text{MC}}_{\text{total}}$	N_{data}
189	36.2	22.4	48.9	58.6	**63**
192	8.5	4.6	54.2	13.1	**15**
196	25.1	14.0	55.3	39.1	**32**
200	23.1	15.0	54.6	38.1	**32**
202	9.6	9.2	55.0	16.8	**23**

Table 5.2: The selection results for hadronic single-W events, where a lower cut value of 0.3 on the discriminating variables has been chosen for illustrative purposes. For the fitting procedure, close to the full range of events, with discriminating values of 0.05 and above, are used as input.

$E_{\text{c.m.}}$(GeV)	lepton	$N^{\text{MC}}_{\text{background}}$	$N^{\text{MC}}_{\ell\nu(e)\nu\text{signal}}$	Efficiency (%)	$N^{\text{MC}}_{\text{total}}$	N_{data}
189	e	6.8	6.9	53.6	12.7	**10**
	μ	3.0	6.4	67.3	9.4	**7**
	τ	1.4	1.6	19.0	3.1	**2**
192	e	1.4	1.2	53.6	2.6	**4**
	μ	0.7	1.0	64.7	1.7	**1**
	τ	0.2	0.3	19.7	0.5	**1**
196	e	2.8	3.6	52.7	6.4	**3**
	μ	1.4	3.2	65.2	4.5	**4**
	τ	0.5	0.9	20.0	1.4	**3**
200	e	3.0	3.9	53.3	6.9	**9**
	μ	1.3	3.2	63.3	4.5	**2**
	τ	0.7	1.0	20.3	1.7	**1**
202	e	1.2	1.8	53.2	3.0	**5**
	μ	0.6	1.5	63.3	2.0	**1**
	τ	0.3	0.4	20.3	0.7	**0**

Table 5.3: The selection results for leptonic single-W events.

5.2 Coupling Measurements

In this section, the results for gauge coupling likelihoods and allowed regions are shown. Where not noted, the results are for a combination of all channels and all centre-of-mass energies that have

been discussed previously. The first two sections describe the results under the scenarios where gauge invariance is realised linearly and non-linearly. while other combinations of couplings are shown in the section which follows.

Single couplings plots are shown in negative log likelihood form, where the 68% confidence level is at $-\log L = 0.5$ when the curves can be approximated by parabola. Two-couplings plots are plotted with exclusion curves representing 68.27%, 95.45% and 99.0% confidence level boundaries. According to convention, these are donoted as 68%, 95% and 99% C.L. curves in the plots for brevity. All curves include statistical, systematic and theoretical errors.

Linear Realisation Model

In the scenario where gauge invariance is realised linearly (cf. Section 1.3), the three couplings $g_1^Z, \kappa_\gamma, \lambda_\gamma$ are allowed to vary, while the other couplings satisfy the relations of Eq. 1.19, and g_5^Z is held at its SM value of zero.

Single Couplings

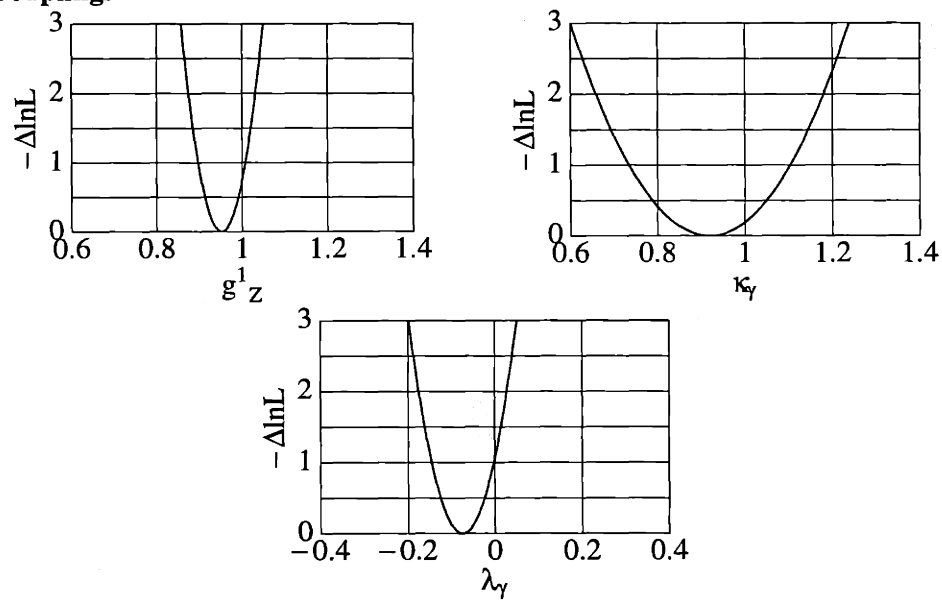

Multiple Couplings

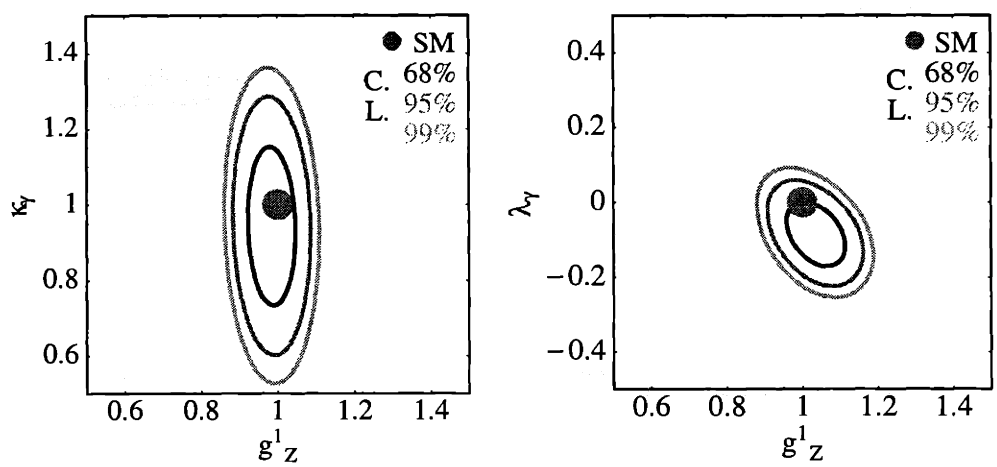

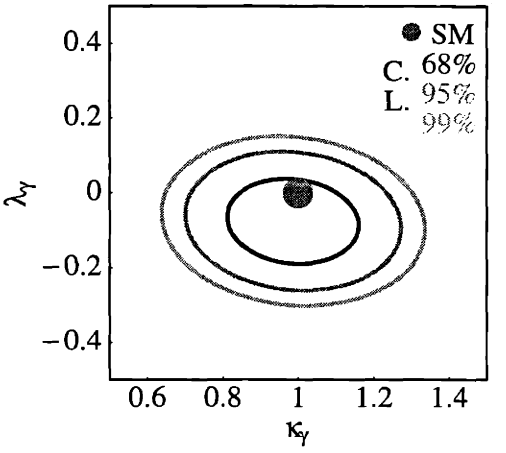

Nonlinear Realisation Model

In the non-linear model, signs of New Physics appear in the set of couplings $\{\Delta g_1^Z, \Delta\kappa_\gamma, \Delta\kappa_Z, g_5^Z\}$, and the others assume their SM values.

Single Couplings

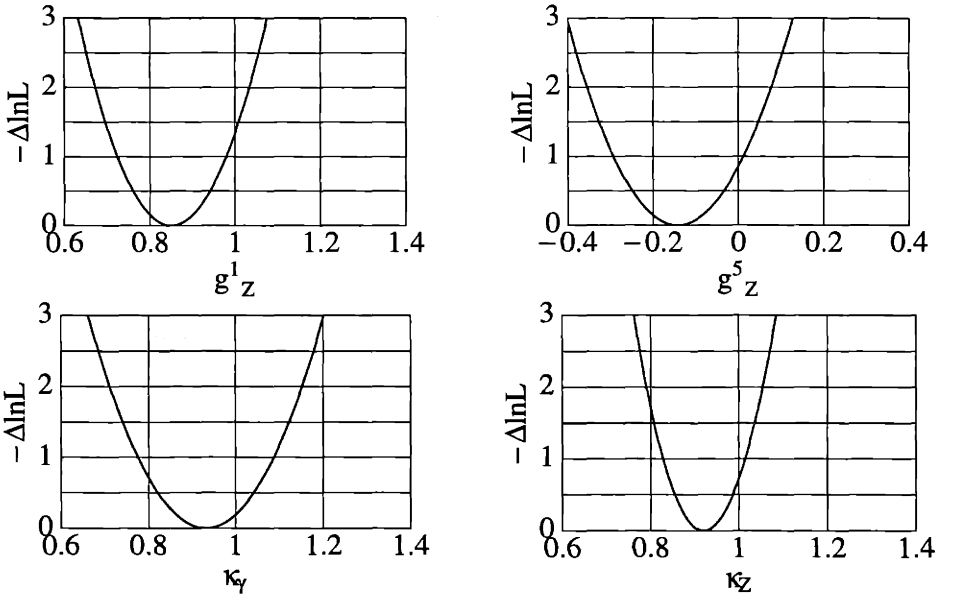

Multiple Couplings

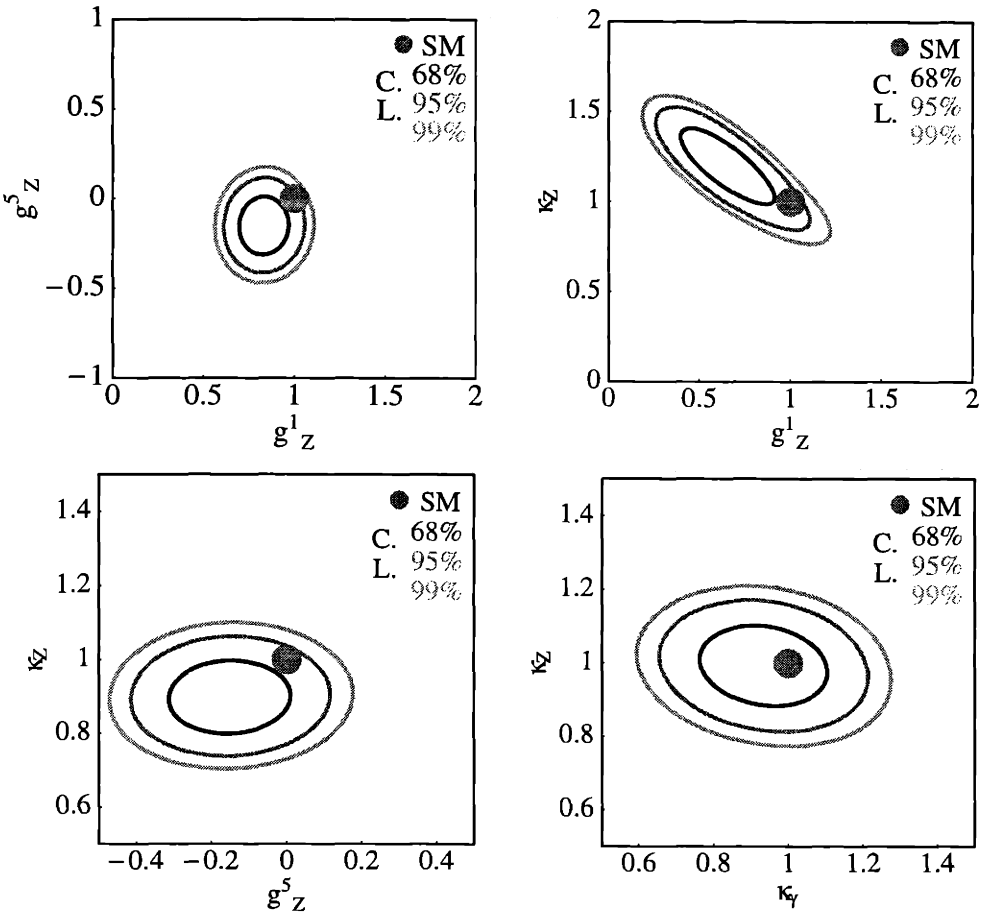

Other Coupling Fits

While the above models provide insight into which couplings would be the most sensitive to possible effects of New Physics, it is equally important to measure the couplings under generalised assumptions. Here, results from the fits for combinations of the remaining couplings are shown.

Single Couplings

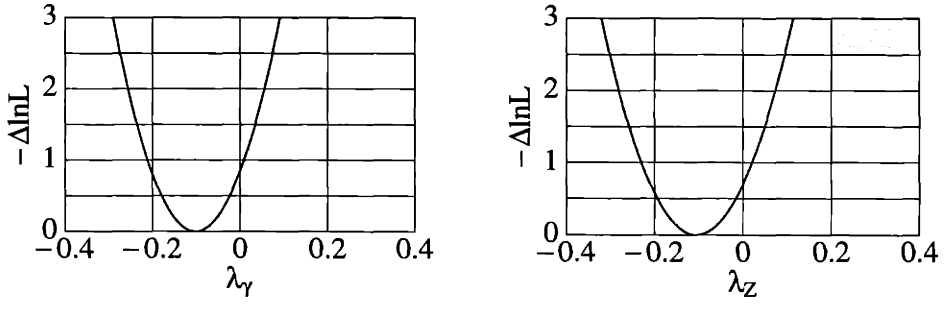

Multiple Couplings

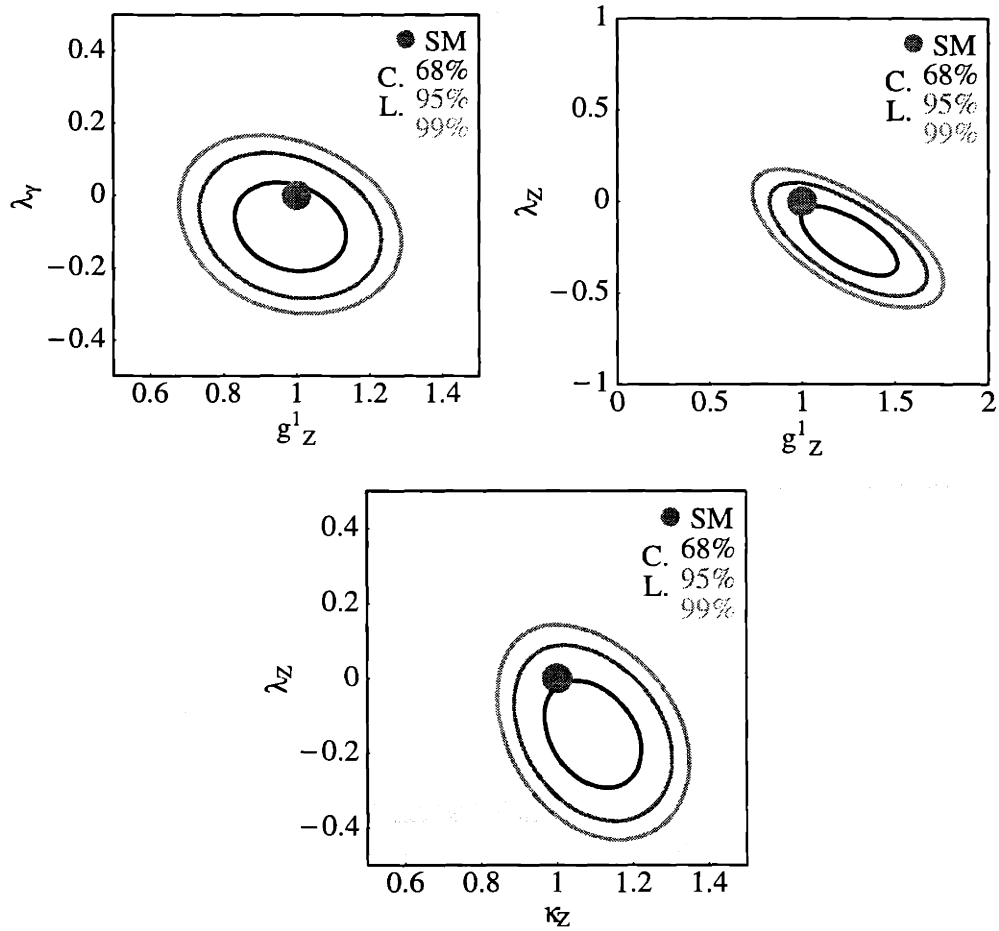

Numerical Results and Comparisons

The single coupling fit results are summarised numerically in Table 5.4.

Model	Coupling		Stat.		Syst.	Theo.
Linear	g_1^Z	0.95	-0.03	$+0.03$	± 0.03	± 0.03
	κ_γ	0.91	-0.05	$+0.05$	± 0.10	± 0.07
	λ_γ	-0.07	-0.03	$+0.03$	± 0.03	± 0.03
Non-Linear	g_1^Z	0.85	-0.06	$+0.07$	± 0.03	± 0.06
	κ_γ	0.92	-0.04	$+0.04$	± 0.08	± 0.06
	κ_Z	0.92	-0.05	$+0.05$	± 0.03	± 0.05
	g_5^Z	-0.15	-0.06	$+0.07$	± 0.07	± 0.06
Other Couplings	λ_γ	-0.09	-0.04	$+0.04$	± 0.06	± 0.03
	λ_Z	-0.10	-0.04	$+0.05$	± 0.06	± 0.05

Table 5.4: Numerical results for single couplings. All other couplings are held at their SM values, with the exception of the Linear Realisation Model couplings for which the relations 1.19 hold. Statistical, systematic and theoretical errors are shown at 68% C.L.

These results can be compared to other direct measurements from past and current experiments. Prior to LEP II running, the best direct constraints on couplings came from studies of Wγ events at the CDF and D$\emptyset$ experiments which yielded the results [67–69]

$$-1.6 < \Delta\kappa_\gamma < 1.8, \quad -0.6 < \lambda_\gamma < 0.6. \quad (95\%\text{C.L.})$$

for the $WW\gamma$ couplings.

The preliminary combined LEP results for the couplings in the linear model as of the summer of the year 2000, including data up to 202 GeV are [70]

$$-0.077 < \Delta g_1^Z < 0.030 \quad -0.130 < \Delta\kappa_\gamma < 0.130$$
$$-0.094 < \lambda_\gamma < 0.024. \qquad (95\%\text{C.L.})$$

The results obtained in this thesis are fully compatible with both the Standard Model expectations and all other reported measurements.

Chapter 6 — Conclusions

The production of W bosons from electron-positron collisions of centre-of-mass energies of 189-202 GeV has been studied using the L3 detector at LEP II. Events from all W production and decay channels are selected, with the luminosity collected over all energies of 400 pb^{-1} corresponding to an estimated total of 2254 fully-hadronic, 2187 semi-leptonic, 397 fully-leptonic W-pair signal events, and 63 hadronic 21 leptonic single-W signal events.

A customised selection procedure is used for the semi-leptonic W-pair and hadronic single-W events, and leptonic single-W events. The first two of these event types have event signatures which overlap when the leptons in semi-leptonic events are badly reconstructed, which is taken into consideration in the selection algorithm.

The W boson production cross sections and shape distributions of these events are used to measure the couplings factors in the generalised expression for the three gauge boson vertices involving two W's and a Z or a photon. While models which provide justification for reducing the number of free couplings are considered, more general fits with fewer constraints are performed to allow model independent sensitivity to possible signs of new physics. Results of simultaneous fits to many combinations of two parameters are also shown to this effect.

While the W-pair cross sections are higher than that of the single-W processes by more than an order of magnitude, events from the latter category are useful in that they provide information which allows the WWZ and $WW\gamma$ contributions to the full vertex couplings to be disentangled. The combination of constraints from the different processes are incorporated into the results using a method which assures that double counting of events across these categories which form mutually irreducible forms of background does not occur, without the introduction of arbitrary cuts to differentiate between categories.

The Standard Model of Electroweak Physics has very specific predictions for the values that these couplings must take, originating from self consistency arguments within the model as a gauge theory. The boson coupling values measured in this way can also act as indirect indicators of New Physics, which occurs at energies higher than those that can be probed by more direct methods. Loop effects due to New Physics have the potential to alter the measured coupling values, and the results presented here can be used to obtain limits on theories which predict such effects.

The coupling values measured here show good consistency with the values predicted by the Standard Model, indicating that triple gauge boson interactions are consistent with their description as those of bosons in a gauge theory.

The full LEP II data set will provide over half as much data again, and the combination of results from all four LEP experiments will allow the couplings to be determined to approximately $\mathcal{O}(10^{-2})$ at 68% C.L. In order to fulfill this possibility, much research is being conducted into improving the theoretical modelling of the signal and background processes involved in measurements of the gauge couplings. Additionally, the high integrated luminosities which will be gathered at the upcoming hadron colliders, the Tevatron and LHC, and at future 500 GeV to 1.5 TeV linear electron positron colliders should allow the measurement of these couplings to up to $\mathcal{O}(10^{-4})$ at 95% C.L. [26], and can be expected to provide a complementary contribution to those of direct searches in investigating the structure of particles and their interactions at TeV levels.

Appendix A — Gauge Boson Coupling Notation

The naming scheme for gauge boson couplings given in Chapter 1.3 is one of several that have been in common use over the last few decades. The two most commonly encountered of these are summarised here.

One set of couplings is defined in reference [71]:

$$x_\gamma = \Delta\kappa_\gamma \tag{A.1a}$$
$$y_\gamma = \lambda_\gamma \tag{A.1b}$$
$$\delta_z = \Delta g_1^Z \cot\theta_W \tag{A.1c}$$
$$x_z = (\Delta\kappa_Z - \Delta g_1^Z)\cot\theta_W \tag{A.1d}$$
$$y_z = \lambda_Z \cot\theta_W \tag{A.1e}$$

The number of couplings being limited by the relations

$$x_z = -x_\gamma \tan\theta_W \tag{A.2a}$$
$$y_z = y_\gamma \cot\theta_W. \tag{A.2b}$$

Another set is designed to parametrise couplings which were least constrained by pre-LEP II data. This set naturally follows from the linear realisation scenario of new physics.

$$\alpha_{B\phi} = x_\gamma - \delta_z \sin\theta_W \cos\theta_W \tag{A.3a}$$
$$= \Delta\kappa_\gamma - \Delta g_1^Z \cos^2\theta_W \tag{A.3b}$$
$$\alpha_{W\phi} = \delta_z \sin -\theta_W \cos\theta_W \tag{A.3c}$$
$$= \Delta g_1^Z \cos^2\theta_W \tag{A.3d}$$
$$\alpha_W = y_\gamma \tag{A.3e}$$
$$= \lambda_\gamma \tag{A.3f}$$

The terms in the effective Lagrangian at the electroweak scale which remain after assuming $SU(2)\times U(1)$ gauge invariance at the new physics scale and considering only terms which do not cause significant deviations in indirect TGC measurements can be written (cf. Eq. 1.18)

$$\mathcal{L}_{d=6}^{TGC} = i g' \alpha_{B\phi}(D_\mu\Phi)^\dagger B^{\mu\nu}(D_\nu\Phi)M_W^2 + i g\, \alpha_{W\Phi}(D_\mu\Phi)^\dagger \boldsymbol{\tau}\cdot \boldsymbol{W}^{\mu\nu}(D_\nu\Phi)M_W^2 + g\, \alpha_W \boldsymbol{W}_\nu^\mu \cdot (\boldsymbol{W}_\rho^\nu \times \boldsymbol{W}_\mu^\rho)/6M_W^2,$$

which provides the motivation for the definition of the coupling parameters.

Appendix B — Four Fermion Processes

The signal processes of interest represent various subclasses of the full set of processes which have four fermion final state particles. The simplest, and most central is the 'CC03' class, which is discussed in Section 3.1. The number of tree-level diagrams contributing to processes with final states particles with are identical to those which can result from W-pair production ranges from nine for the $\mu^-\bar{\nu}_\mu\tau^+\nu_\tau$ channel to 56 for the $e^-\bar{\nu}_e e^+\nu_e$ final state.

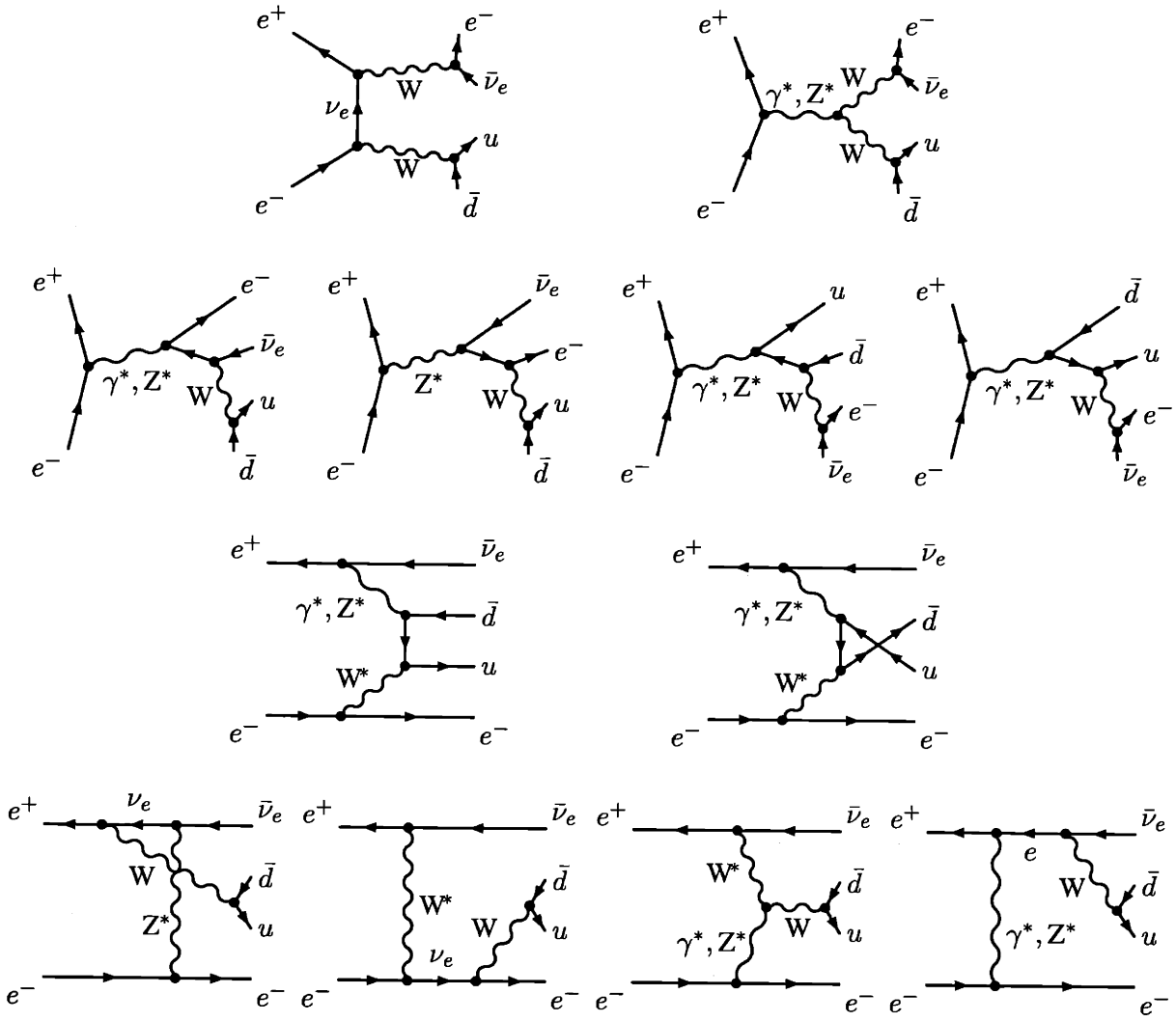

Figure B-1: The 'CC20' class of diagrams. The first row is the double-resonant 'CC03' set, the second row consists of the seven diagrams which complete the set of s-channel diagrams, and the remaining diagrams are the t-channel diagrams, of which the six in the last row are single-resonant.

In this section, the subclasses which are relevant to the analysis are introduced. The practical issues surrounding the calculation of matrix elements and event distributions for these processes are reviewed elsewhere [66].

Fig. B-1 lists the twenty Feynman diagrams representing the process $e^{\pm} \to e\bar{\nu}_e u\bar{d}$ belonging the 'CC20' class. These form the tree-level diagrams which are required to calculate the matrix elements for four-fermion processes with a single electron, a neutrino and a quark pair in the final state. Processes with a muon or tau with its neutrino instead of the quark pair have a similar set of eighteen diagrams, with the two 'CC20' diagrams corresponding to those which involve photon-u vertices in the hadronic processes being missing for $e\bar{\nu}_e\nu_\mu\mu^+$ due to the absence of photon-neutrino couplings.

While the double-resonant 'CC03' diagrams are dominant for W-pair production processes, the full 'CC20' set of diagrams needs to be considered for events where the electron remains very close to the beam pipe, ie, for single-W events. MC events generated using the full 'CC20' calculations

are used for the semi- and fully-leptonic channels in the single-W production regions of phase space where the 'CC03' approximation does not hold, whereas the 'CC03' calculations are retained for the remaining regions. The calculations of the contributions from diagrams which are not double resonant (cf. Section C.3) allow the extraction of underlying coupling information from data events found in these phase space regions.

Appendix C — Implementation Details

C.1 Event Selection

The selection algorithms and the physics reasons behind them are summarised in this section.

Characteristics of Background Processes

In the following sections, the characteristics of the main background processes for this study are listed. Cross sections quoted are for 200 GeV centre-of-mass energy.

Z Pair

The cross section for Z pair production rise rapidly above the production threshold energy of 182GeV, but is still relatively low at LEP II energies (1.26 pb). In spite of this, the approximately 30% of events which are of the form of a Z decaying into two quarks, and the other evading detection by decaying into two neutrinos, is a source of nearly irreducible background to $qq(e)\nu$ events. Due to the difficulty in charge-tagging quarks jets, the fact that W-decay products add up to unit charge while combined decay products of a Z are neutral is difficult to use as a discriminating factor. The invariant masses of the decay products differ by 10 GeV, which is similar to the experimental resolution, and the width of a few GeV of the bosons reduce the effectiveness of this parameter as a discriminant. At the energies under consideration, the Z bosons are much more likely to be produced at rest than the W's, which are well above threshold, so the velocity of the jet pair combination, as measured from their momentum and energy, provides a reasonable discriminating observable. The combination of the above allows the separation of Z and W events.

Zee

Zee events (3.52 pb) are a source of background for both hadronic and leptonic signal processes, since the Z can decay hadronically, mimicking a W event if one of the electrons is lost, or leptonically or into neutrinos which results in an event with two low energy electrons, which can appear to be a leptonic single-W event if only one electron is visible. These forms of background are reduced by putting cuts on excess energy deposits for hadronic Z decays, or taking advantage of the difference in kinematics with the signal leptons by inserting a lower bound on the lepton energies for Z decays into neutrinos.

Quark Pair

Two fermion processes have high cross sections at LEP II and it follows that the cross section for such events with large undetected ISR is also high. For $e^+e^- \rightarrow Z^*/\gamma^* \rightarrow qq(\gamma)$ events the value is 85.5 pb . These radiative events are characterised by missing energy and asymmetric hadron jets, which can be similar in nature to the hadronic W-decay processes which form one of the signals processes for this analysis. The most significant distinguishing feature is the fact that the energy lost due to ISR is in the direction of the incoming beams to an overwhelming degree. Thus the events appear symmetric in the $r - \phi$ plane, and the acollinearity of the two jets in this plane and the small angle between the beams and the missing momentum vector is used to differentiate these

event from the signals, which are more unbalanced due to the energy and momentum lost to an undetected neutrino, which can be in any direction.

W Pair

For the $qq\ell\nu$ selection, the WW $\rightarrow$ $qqqq$ process (8.14 pb) also acts as a minor source of background events. Two jets in a fully hadronic event which are in the same direction can appear as a single jet to the detector, or a jet can be largely in the direction of the beam pipe, making it more difficult to reconstruct. Here, the effect of such events as background is seen as a small number of events in the region of the $qq\ell\nu$ neural network output distribution below 0.05 and is rendered negligible by the event weighting procedure.

Two Photon Interactions

At LEP II energies, interactions between photons emitted from the electrons and positrons in the beams are a source of a significant fraction of the events observed. Most of these events have a small number of low energy particles, but some contain particles with high enough energies to become a background for the processes studied here. This category of event is not as well modelled by MC generators, and for hadronic events, taking the output of PHOJET [72] without corrections introduces significant excesses compared to data.

Here, this correction is performed by producing an event selection identical to the one to be used for fitting but with the requirement that the visible energy in the event be large, which is is intended to reduce the two photon interaction background, being omitted. Inspection of the distributions of the results of this selection indicate that it can be considered as a sample of events with a high fraction of signal events but with the discrepancy due to bad modelling of the two photon events maximised. The cross section of the two photon interaction contribution is then varied to fit the data, and the ratio of the fitted value of the cross section and the expected value from the MC is taken as the correction factor. The errors introduced by this process are minimised by employing a tight cut of 60 GeV as the lower bound on the visible energy to reduce the two photon contribution in the final selection. The uncertainty on the measurements due to the modelling of these events is significantly smaller than the better known theoretical uncertainties on the other processes, and is included as a systematic error.

DIAG36 [73] is used to simulate leptonic two photon events, which appear as background in the leptonic single-W selections.

Selection Cuts

The above requirements for the events selections are incorporated into the selection cuts which are listed below.

The cut values used for the $2j1\ell$ and $2j$ selection are listed in Table C.1. The method by which these cuts are applied to provide a selection for the two event categories is described in Section 3.3. The cuts used to select leptonic single-W events are shown in Table C.2.

The selection criteria for the other channels use the standard L3 cuts and are summarised in Refs. [49].

Artificial Neural Network

The artificial neural network package JETNET 3.5 [60] is used. The results are not sensitive to the specific learning algorithm. Here, Langevin learning with a single hidden layer of nodes is chosen.

As described in Section 3.3, two neural networks are used. The first, which takes events reconstructed as two hadronic jets, separates between WW $qq\ell\nu$ events with a badly reconstructed lepton, and hadronic single-W events, and non-coupling dependent background events. The quantities fed

		Cut Quantity		
2	$\leq$	no. scintillator hits‡		
		$\lvert\cos(\theta_{\not p})\rvert$ ($\not p$: missing momentum vector)‡	$<$	0.99
		energy in luminosity monitor‡ [GeV]	$<$	65.0
		energy in active lead ring‡ [GeV]	$<$	20.0
8	$\leq$	no. calorimetric clusters	$\leq$	65
5	$\leq$	no. detector-wide tracks	$\leq$	45
5	$\leq$	no. good central tracks	$\leq$	35
		no. well reconstructed muon tracks	$\leq$	2
8.0	$<$	transverse momentum [GeV]		
		acoplanarity [rad]	$<$	3.05
		acollinearity [rad]	$<$	2.95
$50.0 \times \sqrt{s}$	$<$	visible energy [GeV]	$<$	$0.80 \times \sqrt{s}$
30.0	$<$	invariant mass [GeV]	$<$	140.0
10.0	$<$	energy in ECAL [GeV]	$<$	$0.40 \times \sqrt{s}$
		sum of jet invariant masses[GeV]	$<$	75.0
		energy in 25° sector around missing momentum [GeV]	$<$	35.0
		energy in 45° cone opposite two jets [GeV]	$<$	45.0
		energy of most energetic photon [GeV]	$<$	60.0

Table C.1: The cut values used in the $2j1\ell$ and $2j$ selection. (‡ Global preselection cuts.)

to the input nodes are: the Spherocity [74]; the second Fox-Wolfram moment for three particle correlations [75], the velocity of the hadronic system, the acoplanarity of the two jet system; $\cos\theta_{\not p}$, where $\theta_{\not p}$ is the polar angle of the missing momentum vector; $M_{\rm jet}/E_{\rm jet}$ for the third most energetic jet; $M_{\rm jet}/E_{\rm jet}$ for the fourth most energetic jet; the opening solid angle between jets when event is forced to three jets; the transverse momentum; the invariant mass of the entire event; the event b-tag; the maximum jet width; sum of invariant masses of the two jets; difference between invariant masses of the two jets; values of y, the jet algorithm [46,47] distance variable at point when number of jets in event changes from four to three, and three to two.

The second network distinguishes between genuine $qq\ell\nu$ events and background. The input variables are: the energy of the lepton; polar angle of the lepton; the invariant mass of the hadronic system; the invariant mass of the lepton/missing-energy system; the invariant mass of the event with lepton removed; the number of calorimetric clusters, excluding those attributable to the lepton; the χ^2 for a 4C $qq\ell\nu$ kinematic fit; the velocity of hadronic sytem;

Distributions of some of the variables are shown in Fig. C-1. In both cases, each input variable is normalised for centre-of-mass energy and processed to lie in the range $[0, 1]$ prior to use by JETNET. For training, one quarter of the available MC events are used, with the event weights calculated to correspond to the SM expectation. These events are not used for subsequent selection and fitting analyses. A validation set of events is used to check for overlearning but is not used for determining the optimal end-of-training point since the results are seen to be stable beyond a certain number of iterations, and overlearning is not encountered.

Lepton Type			Cut Quantity		
all types	1	$\leq$	no. scintillator hits		
			energy in luminosity monitor / active lead ring [GeV]	$<$	60.0
	15.0	$<$	lepton energy [GeV]		
			visible energy [GeV]	$<$	30.0
			minimum track distance of closest approach [mm]	$<$	1.0
			minimum scintillator timing [ns]	$<$	0.8
			maximum angle between any pair of tracks [rad]	$<$	0.25
	20.0	$<$	E_{lepton}		
electrons			$\lvert\cos\theta_e\rvert$	$<$	0.70
	0.95	$<$	E_e/E_{visible}		
muons			$\lvert\cos\theta_\mu\rvert$	$<$	0.80
	0.92	$<$	E_μ/E_{visible}		
			invariant mass†[GeV]	$<$	0.2
	0.3	$<$	$E_{\text{HCAL}}{}^\dagger$ [GeV]	$<$	4.5
taus			$\lvert\cos\theta_\tau\rvert$	$<$	0.88
	0.93	$<$	$E_\tau/E_{\text{visible}}$		
			energy deposit and closest track $\Delta\phi$	$<$	0.1
	0.5	$<$	fraction of lepton energy within 10° cone		

Table C.2: The cut values used in the leptonic single-W selection. (†Cuts applied in parallel.)

C.2 Distribution Fitting

Validity of Extraction Method

The statistical stability of the fit is tested by taking test sets of Monte Carlo events which have been processed using methods which are identical to that which the data events undergo. These are fed to the fitting algorithm in the same way as the data events, and the results after many repetitions are evaluated to verify that they follow expectations.

Another test of the fitting procedure involves using MC events, which are generated with anomalous values for the couplings to be measured, as 'data' events. This is performed for a variety of anomalous values to ensure the fit produces results which are compatible with the input values of the parameters up to statistical fluctuations. An example of the results of these tests are shown in Fig. C-2.

C.3 Computer Programs

Brief descriptions of the computer programs used in this analysis are given here for completeness.

Selection and Fitting

Two custom written programs are used in this analysis. The first program, in FORTRAN, takes as its input, data and MC event information in the form of both L3 'New Particle Group Ntuples' (npntuples) and L3 'W Physics Group Listfiles' (listfiles). The former contains hundreds of event variables that have been processed in order to facilitate rapid analyses with new particle searches in mind. The latter are provided by individual members of the W Group who have performed event selections, and contain reconstruction/selection details in addition to an array of basic event variables. Portions of the standard W group code are incorporated into the this program, which process-

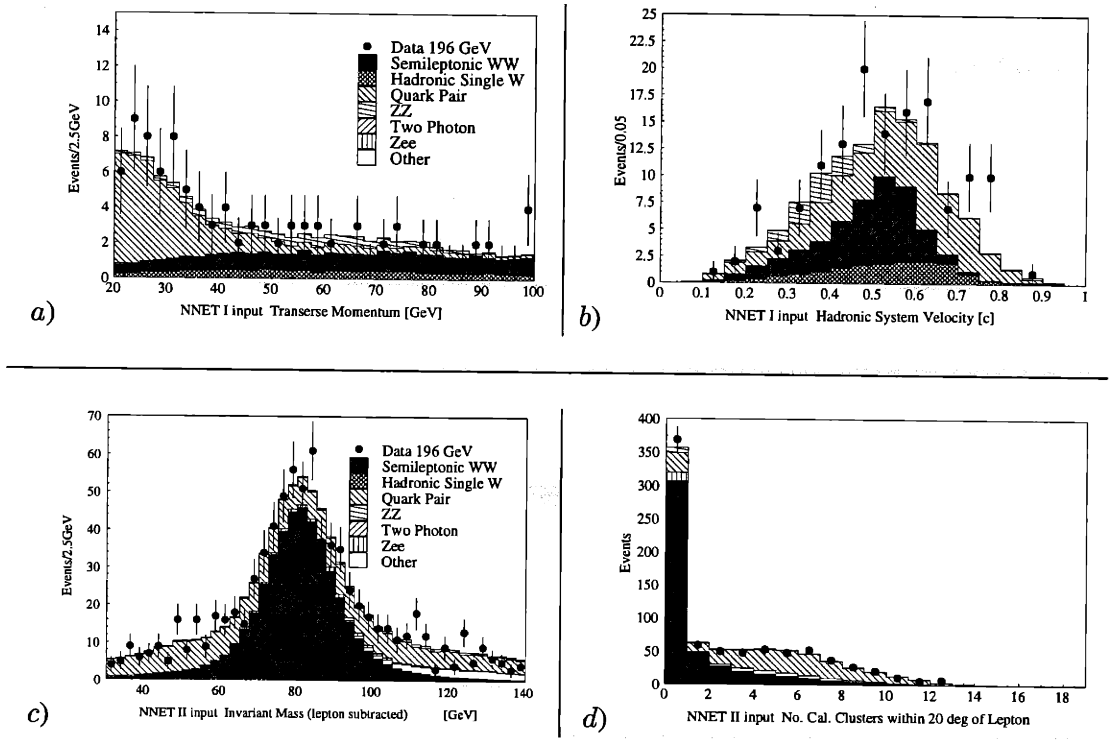

Figure C-1: Selected input variables for the neural networks. NNET I takes events reconstructed with two hadronic jets, and performs a three-way seperation between the background, hadronic single-W events, and W-pair events with a badly reconstructed lepton. Two effective inputs for this network are *a*) the transverse momentum and *b*) the velocity of the hadronic system. NNET II seperates events with two jets and a charged lepton into W-pair events and background. Here the *c*) invariant mass of the remainder of the event after removal of the lepton, and *d*) the number of calorimetric clusters in a 20° cone around the lepton are shown.

es these and outputs them in the form of C++ objects which contain the reconstruction/generation variables and event categorisations used in the fitting process. A suite of C++ classes built upon the ROOT framework [76] is used to process and fit the data. JETNET 3.5 [60] was used for the neural network (cf. Appendix C.1).

Physics Modelling

The following programs are used to provide the physics input for the calculations central to the measurements. Programs listed here but not mentioned elsewhere were used in preliminary studies of the signal or to generate background processes. Full details for these and other programs used for background studies may be found in the references section. A pre-LEP II review [69,77], and a recent recent report from the LEP II-Monte Carlo workshop four fermion working group [66] contain additional information on the programs available for use.

BHWIDE

BHWIDE 1.01 [78] generates radiative large angle Bhabha scattering events using the YFS [79] scheme to produce the radiative photons.

DIAG36

DIAG36 [73] is a generator for four-lepton final state events in electron-positron collisions and is used here to simulate the background in the single lepton channel due to two photon interactions where lepton pairs are created.

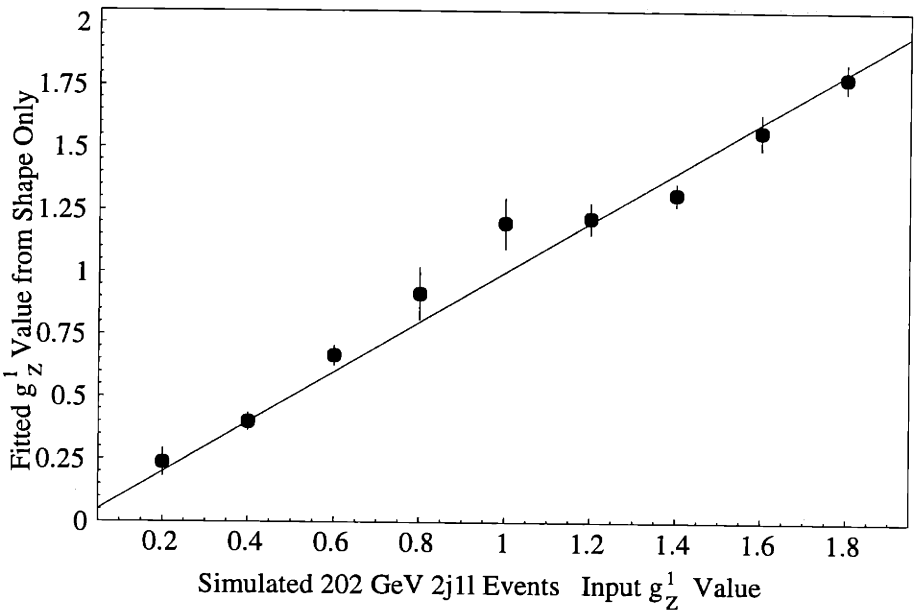

Figure C-2: An example of a test of linearity of the fitting method. The plot shows the distribution of fit results using an 'event shape only' fit for g_1^Z from simulated MC samples using the 202 GeV $2j1\ell$ selection. An input value for the coupling is chosen, and an MC sample is generated with the same number of events as expected in data for the nominal integrated luminosity, with signal to background ratios and event distributions as expected for a data sample with this value for g_1^Z. This is repeated for each value of the input coupling, and the mean of the fit results and their spread is shown in the form of a point and an error bar for each input value.

Excalibur

EXCALIBUR 2.05 [80,81] is MC event generator for all four-fermion processes, which uses massless fermions and zero transverse momentum ISR photons. A recent modification allows the generation of events with an electron with near zero scattering angle, which is in principle not possible for programs utilising the massless approximation for fermions due to singularities which appear in this limit.

Gentle

GENTLE 2.01 [52] allows the semi-analytical calculation of differential cross sections of four-fermion processes, and is used in general to calculate the theoretical ratio of 'CC03' cross sections, and full four-fermion cross sections.

Grc4f

GRC4F 2.1 [82] is a four-fermion event generator with finite fermion masses and inclusion of the W width in such a way as to allow the generation of event over full phase-space without being hindered by unphysical singularities. All tree level diagrams for the 76 four fermion processes are included.

HERWIG

HERWIG [65] is a general purpose event generator, with an emphasis on the detailed simulation of QCD parton showers. Here the showering part is used in conjunction with underlying four fermion events from KORALW, to estimate the effects of fragmentation models on the final results.

JETSET

JETSET 7.4 [51] is a event generator which includes hadronisation using Lund string fragmentation. Here the hadronisation package is used independently to take the particles provided by an event generator and model their evolution into the jets of hadrons seen in the detector.

KORALW

KORALW 1.33 [50] is a MC event generator, specialising in 'CC03' and four-fermion events, which uses the YFS scheme [79] to produce ISR photons with finite transverse momentum, and uses PHOTOS [83] for final state radiation.

KORALZ

KORALZ 4.03 [84] specialises in τ-pair production event generation, with $\mathcal{O}(\alpha^2)$ initial and final state radiation and $\mathcal{O}(\alpha)$ electroweak corrections, and more than twenty distinct τ decay modes. It can also generate fermion pair events with other fermion types, and here it is used for the $\mu\mu$ in addition to the $\tau\tau$ channel.

PHOJET

PHOJET 1.05c [72] is a minimum bias event generator for hadronic two-photon interactions, which uses the Dual Parton Model in terms of reggeon and pomeron exchanges. This is combined with perturbative QCD, allowing both soft and hard scatterings to occur within a single event.

PYTHIA

PYTHIA 5.722 [51] is a general event generator used here to generate the $Z^*/\gamma \rightarrow qq$, Ze^+e^- and $ZZ \rightarrow$ background events.

Bibliography

[1] A. Salam. Weak and Electromagnetic Interactions. Originally printed in *Svartholm: Elementary Particle Theory, Proceedings Of The Nobel Symposium Held 1968 At Lerum, Sweden*, Stockholm 1968, 367-377.

[2] S. Weinberg. A Model Of Leptons. *Phys. Rev. Lett.*, **19** (1967) 1264–1266.

[3] P. A. M. Dirac. The Quantum theory of electron. *Proc. Roy. Soc. Lond.*, **A117** (1928) 610–624.

[4] P. A. M. Dirac. Relativistic wave equations. *Proc. Roy. Soc. Lond.*, **155A** (1936) 447–459.

[5] E. Fermi. An attempt of a theory of beta radiation. 1. *Z. Phys.*, **88** (1934) 161–177.

[6] Hideki Yukawa. On the interaction of elementary particles. *Proc. Phys. Math. Soc. Jap.*, **17** (1935) 48–57.

[7] A. Salam & J. C. Ward. On A Gauge Theory Of Elementary Interactions. *Nuovo Cim.*, **19** (1961) 165.

[8] J. Goldstone. Field Theories With 'Superconductor' Solutions. *Nuovo Cim.*, **19** (1961) 154.

[9] Y. Nambu & G. Jona-Lasinio. Dynamical model of elementary particles based on an analogy with superconductivity. I. *Phys. Rev.*, **122** (1961) 345.

[10] P. W. Higgs. Broken symmetries, massless particles and gauge fields. *Phys. Lett.*, **12** (1964) 132–133.

[11] F. Englert & R. Brout. Broken Symmetry And The Mass Of Gauge Vector Mesons. *Phys. Rev. Lett.*, **13** (1964) 321.

[12] G. S. Guralnik, C. R. Hagen & T. W. B. Kibble. Global Conservation Laws And Massless Particles. *Phys. Rev. Lett.*, **13** (1964) 585.

[13] M. Acciarri *et al.* Higgs candidates in e+ e- interactions at s**(1/2) = 206.6- GeV.

[14] S. L. Glashow. Partial Symmetries Of Weak Interactions. *Nucl. Phys.*, **22** (1961) 579–588.

[15] A. Salam & J. C. Ward. Electromagnetic and weak interactions. *Phys. Lett.*, **13** (1964) 168–171.

[16] Y. Fukuda *et al.* Evidence for oscillation of atmospheric neutrinos. *Phys. Rev. Lett.*, **81** (1998) 1562–1567.

[17] C. Caso *et al.* Review of particle physics. *Eur. Phys. J.*, **C3** (1998) 1–794.

[18] G. Altarelli, R. Barbieri & F. Caravaglios. Electroweak precision tests: A concise review. *Int. J. Mod. Phys.*, **A13** (1998) 1031.

[19] G. Arnison *et al.* Experimental observation of isolated large transverse energy electrons with associated missing energy at s**(1/2) = 540-GeV. *Phys. Lett.*, **B122** (1983) 103–116.

[20] M. Banner *et al.* Observation of single isolated electrons of high transverse momentum in events with missing transverse energy at the CERN anti-p p collider. *Phys. Lett.*, **B122** (1983) 476–485.

[21] K. Hagiwara, R. D. Peccei, D. Zeppenfeld & K. Hikasa. Probing The Weak Boson Sector In e+ e- → W+ W-. *Nucl. Phys.*, **B282** (1987) 253.

[22] K. J. F. Gaemers & G. J. Gounaris. Polarization Amplitudes For e+ e- → W+ W- And e+ e- → Z Z. *Zeit. Phys.*, **C1** (1979) 259.

[23] Aneesh Manohar & Howard Georgi. Chiral Quarks And The Nonrelativistic Quark Model. *Nucl. Phys.*, **B234** (1984) 189.

[24] Stephen Godfrey & Heinz Konig. Atomic parity violation as a probe of anomalous gauge boson couplings. *Phys. Rev.*, **D45** (1992) 3196–3200.

[25] G. Gounaris *et al.* Triple Gauge Boson Couplings. *LEP Yellow Report.*

[26] T. Barklow *et al.* Anomalous gauge boson couplings.

[27] E. N. Argyres, G. Katsilieris, A. B. Lahanas, C. G. Papadopoulos & V. C. Spanos. One loop corrections to three vector boson vertices in the Standard Model. *Nucl. Phys.*, **B391** (1993) 23–41.

[28] G. 't Hooft. Renormalizable Lagrangians For Massive Yang-Mills Fields. *Nucl. Phys.*, **B35** (1971) 167–188.

[29] R. L. Sekulin. Ambiguities in the determination of the vector boson couplings at LEP200. *Phys. Lett.*, **B338** (1994) 369.

[30] C. P. Burgess, Stephen Godfrey, Heinz Konig, David London & Ivan Maksymyk. Bounding anomalous gauge boson couplings. *Phys. Rev.*, **D50** (1994) 7011–7024.

[31] C. Arzt, M. B. Einhorn & J. Wudka. Patterns of deviation from the standard model. *Nucl. Phys.*, **B433** (1995) 41–66.

[32] M. Beccaria, F. M. Renard, S. Spagnolo & C. Verzegnassi. Bounds on anomalous gauge couplings from past and near future experiments: The role of the different measurements. *Phys. Lett.*, **B448** (1999) 129.

[33] K. Hagiwara, S. Ishihara, R. Szalapski & D. Zeppenfeld. Low-energy effects of new interactions in the electroweak boson sector. *Phys. Rev.*, **D48** (1993) 2182–2203.

[34] C. P. Burgess & David London. Uses and abuses of effective Lagrangians. *Phys. Rev.*, **D48** (1993) 4337–4351.

[35] A. De Rujula, M. B. Gavela, P. Hernandez & E. Masso. The Selfcouplings of vector bosons: Does LEP-1 obviate LEP- 2? *Nucl. Phys.*, **B384** (1992) 3–58.

[36] The Construction of the L3 Experiment. *Nucl. Instrum. Meth.*, **A289** (1990) 35.

[37] The LEP Collaborations ALEPH DELPHI L3 OPAL the LEP Electroweak Working Group, the SLD Heavy Flavour & Electroweak Working Groups. A Combination of preliminary LEP electroweak measurements and constraints on the standard model. CERN-EP-2000-016.

[38] M. Sands. The Physics Of Electron Storage Rings: An Introduction. SLAC-0121.

[39] The LEP 2 Team. LEP DESIGN REPORT: VOL. 3. LEP II. CERN-AC/96-01(LEP2).

[40] M. Acciarri *et al.* The L3 Silicon Microvertex Detector. *Nucl. Instrum. Meth.*, **A351** (1994) 300–312.

[41] H. Akbari *et al.* The L3 vertex detector: Design and performance. *Nucl. Instrum. Meth.*, **A315** (1992) 161.

[42] G. Chiefari *et al.* Muon Detection in the L3 Experiment at LEP. *Nucl. Instrum. Meth.*, **A277** (1989) 187.

[43] A. Adam *et al.* The Forward Muon Detector of L3. *Nucl. Instrum. Meth.*, **A383** (1996) 342.

[44] R. Sumner. The L3 BGO Electromagnetic Calorimeter. *Nucl. Instrum. Meth.*, **A265** (1988) 252.

[45] O. Adriani *et al.* Hadron calorimetry in the L3 detector. *Nucl. Instrum. Meth.*, **A302** (1991) 53–62.

[46] N. Brown & W. Stirling. Finding jets and summing soft gluons: A New algorithm. *Z. Phys.*, **C53** (1992) 629–636.

[47] W. Bartel *et al.* Experimental Studies on Multi-Jet Production in e+ e- Annihilation at PETRA Energies. *Z. Phys.*, **C33** (1986) 23.

[48] M. Acciarri *et al.* Measurement of mass and width of the W boson at LEP. *Phys. Lett.*, **B454** (1999) 386.

[49] M. Acciarri *et al.* Measurement of W pair cross sections in e+ e- interactions at s**(1/2) = 183-GeV and W decay branching fractions. *Phys. Lett.*, **B436** (1998) 437.

[50] S. Jadach, W. Placzek, M. Skrzypek, B. F. L. Ward & Z. Was. Monte Carlo program KoralW 1.42 for all four-fermion final states in e+ e- collisions. *Comput. Phys. Commun.*, **119** (1999) 272–311.

[51] Torbjorn Sjostrand. High-energy physics event generation with PYTHIA 5.7 and JETSET 7.4. *Comput. Phys. Commun.*, **82** (1994) 74–90.

[52] D. Bardin *et al.* GENTLE/4fan v. 2.0: A program for the semi-analytic calculation of predictions for the process e+ e- $\rightarrow$ 4f. *Comput. Phys. Commun.*, **104** (1997) 161.

[53] Preliminary Results on the Measurement of W-Pair Cross Sections in e+e- Interactions at sqrt(s)=192-202 GeV and W-Decay Branching Fractions. *L3 Internal Note 2514.*

[54] M. Acciarri *et al.* Production of single W bosons in e+ e- interactions at 130- GeV ¡= s**(1/2) ¡= 183-GeV and limits on anomalous W W gamma couplings. *Phys. Lett.*, **B436** (1998) 417–427.

[55] M. Acciarri *et al.* Production of single W bosons at s**(1/2) = 189-GeV and measurement of W W gamma gauge couplings. *Phys. Lett.*, **B487** (2000) 229–240.

[56] Toshio Tsukamoto & Yoshimasa Kurihara. Single W production to test triple gauge boson couplings at LEP. *Phys. Lett.*, **B389** (1996) 162–168.

[57] F. A. Berends & Geoffrey B. West. Production of single W mesons in electron - positron colliding beams and in electron or muon scattering experiments. *Phys. Rev.*, **D1** (1970) 122.

[58] Y. Kurihara, D. Perret-Gallix & Y. Shimizu. e+ e- → e- anti-electron-neutrino u anti-d from LEP to linear collider energies. *Phys. Lett.*, **B349** (1995) 367–374.

[59] Ernestos N. Argyres *et al.* Stable calculations for unstable particles: Restoring gauge invariance. *Phys. Lett.*, **B358** (1995) 339–346.

[60] Carsten Peterson, Thorsteinn Rognvaldsson & Leif Lonnblad. JETNET 3.0: A Versatile artificial neural network package. *Comput. Phys. Commun.*, **81** (1994) 185–220.

[61] M. D. Richard & R. P. Lippmann. Neural Network Classifiers Estimate Bayesian *a postieriori* Probabilities. *Neural Comput.*, **3** (1991) 461.

[62] G. K. Fanourakis, D. Fassouliotis, A. Leisos, N. Mastroyiannopoulos & S. E. Tzamarias. Multidimensional binning techniques for a two parameter trilinear gauge coupling estimation at LEP II. *Nucl. Instrum. Meth.*, **A430** (1999) 455.

[63] Gerson Goldhaber, Sulamith Goldhaber, Wonyong Lee & Abraham Pais. Influence of Bose-Einstein statistics on the antiproton proton annihilation process. *Phys. Rev.*, **120** (1960) 300–312.

[64] Gosta Gustafson, Ulf Pettersson & P. M. Zerwas. Jet final states in w w pair production and color screening in the QCD vacuum. *Phys. Lett.*, **B209** (1988) 90.

[65] G. Marchesini *et al.* HERWIG: A Monte Carlo event generator for simulating hadron emission reactions with interfering gluons. Version 5.1 - April 1991. *Comput. Phys. Commun.*, **67** (1992) 465–508.

[66] Martin W. Grunewald *et al.* Four-Fermion Production in Electron-Positron Collisions.

[67] F. Abe *et al.* Limits on W W Z and W W gamma couplings from W W and W Z production in p anti-p collisions at s**(1/2) = 1.8-TeV. *Phys. Rev. Lett.*, **75** (1995) 1017–1022.

[68] S. Abachi *et al.* Measurement of the W W gamma gauge boson couplings in p anti-p collisions at s**(1/2) = 1.8-TeV. *Phys. Rev. Lett.*, **75** (1995) 1034–1039.

[69] D. Bardin *et al.* Event generators for W W physics.

[70] S. Jezequel. Charged Triple Gauge Coupling at LEP, talk given at ICHEP 2000, Osaka, Japan.

[71] M. Bilenkii, J. L. Kneur, F. M. Renard & D. Schildknecht. Trilinear couplings among the electroweak vector bosons and their determination at LEP200. *Nucl. Phys.*, **B409** (1993) 22–68.

[72] R. Engel. Photoproduction within the two component dual parton model. 1. Amplitudes and cross-sections. *Z. Phys.*, **C66** (1995) 203–214.

[73] F. A. Berends, P. H. Daverveldt & R. Kleiss. Complete lowest order calculations for four lepton final states in electron - positron collisions. *Nucl. Phys.*, **B253** (1985) 441.

[74] Howard Georgi & Marie Machacek. A Simple QCD prediction of jet structure in e+ e- annihilation. *Phys. Rev. Lett.*, **39** (1977) 1237.

[75] Geoffrey C. Fox & Stephen Wolfram. Observables for the analysis of event shapes in e+ e- annihilation and other processes. *Phys. Rev. Lett.*, **41** (1978) 1581.

[76] R. Brun & F. Rademakers. ROOT: An object oriented data analysis framework. *Nucl. Instrum. Meth.*, **A389** (1997) 81.

[77] Leif Lonnblad *et al.* $\gamma\gamma$ Event Generators.

[78] S. Jadach, W. Placzek & B. F. L. Ward. BHWIDE 1.00: O(alpha) YFS exponentiated Monte Carlo for Bhabha scattering at wide angles for LEP1/SLC and LEP2. *Phys. Lett.*, **B390** (1997) 298–308.

[79] S. Jadach, W. Placzek, M. Skrzypek & B. F. L. Ward. Gauge invariant YFS exponentiation of (un)stable W+ W- production at and beyond LEP2 energies. *Phys. Rev.*, **D54** (1996) 5434–5442.

[80] F. A. Berends, R. Pittau & R. Kleiss. All electroweak four fermion processes in electron - positron collisions. *Nucl. Phys.*, **B424** (1994) 308–342.

[81] F. A. Berends & A. I. van Sighem. Anomalous four fermion processes in electron - positron collisions. *Nucl. Phys.*, **B454** (1995) 467–484.

[82] J. Fujimoto *et al.* grc4f v1.1: a Four-fermion Event Generator for e+e- Collisions. *Comput. Phys. Commun.*, **100** (1997) 128–156.

[83] Elisabetta Barberio & Zbigniew Was. PHOTOS: A Universal Monte Carlo for QED radiative corrections. Version 2.0. *Comput. Phys. Commun.*, **79** (1994) 291–308.

[84] S. Jadach, B. F. L. Ward & Z. Was. The Monte Carlo program KORALZ, version 4.0, for the lepton or quark pair production at LEP / SLC energies. *Comput. Phys. Commun.*, **79** (1994) 503–522.